

Toward target recognition from synthetic aperture radar imagery using electromagnetics-based signatures

Chen-Pang Yeang

Massachusetts Institute of Technology
Laboratory for Information and Decision
Systems
Cambridge, Massachusetts 02139
E-mail: cpyeang@mit.edu

Choongyeun Cho, MEMBER SPIE

Massachusetts Institute of Technology
Department of Electrical Engineering and
Computer Science
Cambridge, Massachusetts 02139

Jeffrey H. Shapiro, MEMBER SPIE

Massachusetts Institute of Technology
Department of Electrical Engineering and
Computer Science
Cambridge, Massachusetts 02139

Abstract. We develop a theory of target detection and classification from physics-based synthetic aperture radar (SAR) signatures. The target-return and clutter-return models are developed from electromagnetic theory. Both stripmap-mode and spotlight-mode SARs are treated. Adaptive-resolution processors, conventional SAR processors, and optimum likelihood-ratio target detectors are presented for multicomponent target detection, and their receiver operating characteristics are compared. Similarly, conventional and optimum likelihood-ratio processors are used for multicomponent target classification. We develop upper and lower bounds and present Monte Carlo simulations for the probabilities of correct classification. © 2003 Society of Photo-Optical Instrumentation Engineers. [DOI: 10.1117/1.1579031]

Subject terms: target detection; target classification; Neyman-Pearson processor; electromagnetic scattering.

Paper 020427 received Sep. 27, 2002; revised manuscript received Dec. 17, 2002; accepted for publication Dec. 20, 2002.

1 Introduction

In recent years, synthetic aperture radars (SARs) have been used to detect manmade targets and distinguish them from naturally occurring backgrounds. A SAR-based automated target recognition (ATR) system requires a fast and effective discriminator to suppress natural clutter, detect the presence of a target, and classify the type of target from its radar return.¹ Such a system relies on models for different components of radar returns, namely, the returns from (different types of) manmade targets, natural clutter, and background noise. One typical approach is to model the target return as a parametrized deterministic signal pattern, and the clutter and noise as stochastic processes characterized by their statistics. In Ref. 2, the clutter and noise are modeled as Gaussian random processes with given covariance matrices, and the target return is modeled as a prespecified spatiotemporal pattern multiplied by complex-amplitude parameters. In Ref. 3, the target return is composed of contributions from several scattering centers. Each scattering-center component contains an amplitude and a phase determined by the radar's carrier frequency and look angle, plus the scattering position centers. The unwanted part of the radar return, i.e., the noise, is assumed to be a white Gaussian process. In Ref. 4, the target signal is taken to be a Gaussian intensity function, the clutter a sinusoid with random phase, and the noise a Gaussian process.

Another approach to radar-signal modeling is to assume that the target return and the unwanted part (clutter plus noise) are random processes characterized by different statistics. In Ref. 5, the target return has deterministic and random parts, with the latter arising from scattering-amplitude and scattering-center uncertainties. In Ref. 6, the radar signal is a target return multiplied by an uncorrelated speckle noise, whose covariance matrices are estimated by

principal-component analysis. This approach presumes that different clutter types have different statistics. The work in Ref. 7 models the full polarimetric radar clutter as the product of a gamma-distributed textural variable and a Gaussian random vector, whose covariance matrix is determined empirically. The numerical values for the covariance-matrix elements calculated from real SAR data are different for trees, shadows, grass, and mixed scrub. In Refs. 8 and 9, each pixel of a SAR image corresponding to a specific type of target at a given pose is modeled as the sum of two mutually independent Gaussian random vectors that represent target return and white noise. The target pose and type are estimated by maximizing the likelihood ratio of the joint conditional Gaussian probability density.

The preceding approaches can also be applied to multiple radar images, i.e., to images of the same scene obtained from different sensors and/or at different resolutions. The signal model in Ref. 10 generalizes that of Ref. 2 by making each image point a vector, whose components represent sensor data collected at different bandwidths. In Refs. 11 and 12, radar images at different resolutions are modeled as Markov random fields, and the parameter values in their statistical models are used as the basis for classification or texture segmentation.

Recent studies of multiresolution radar images have revealed promising potential for solving target identification problems. The work in Ref. 13 shows that a processor based on an autoregressive model of multiresolution millimeter-wave SAR imagery provides useful discrimination between natural clutter and manmade targets. In Ref. 14, ultra-wide-band (UWB) foliage-penetrating SAR data demonstrated that adaptive-resolution imaging can exploit the aspect-dependent reflectivity of manmade objects. Reference 15 shows that discrimination can be accomplished

via adaptive multiresolution processing based on the different variation-versus-resolution patterns of targets and clutter.

The aforementioned treatments are founded more on provisional signal models than on rigorous, physics-based theory. In particular, they do not take into account the effects of transmitter pulse shape, antenna beam patterns, and free-space wave propagation that relate the radar return from targets and clutter to their respective physical characteristics via an electromagnetic scattering model. In Refs. 16 and 17, the return signals corresponding to spotlight-mode and stripmap-mode SARs are constructed via a comprehensive consideration of radar-pulse transmission and propagation. The resultant return signal is formulated as a spatial integral of a Lambertian reflectivity pattern within the region of interest and the Green's function corresponding to the mode of radar operation. This approach, however, is not directly derived from a rigorous electromagnetic scattering theory, and therefore does not capture certain important features, such as aspect-angle dependence, in the return from a specular object. The work in Ref. 18 claims to build a physics-based model for the UWB radar return of a specular target, from an observed fact that a UWB pulse incident on a flat reflector produces two return pulses, because of the discontinuities at the reflector's edges. This phenomenon, although predictable from scattering theory, can fail to capture other significant features in the radar return. In Refs. 19 and 20, a target-return model for UWB SAR is constructed from physical optics and the physical theory of diffraction. The pulse shape is taken from the UWB specification, and the antenna beam pattern, although not included, could be incorporated by multiplying the return by a location-dependent weighting function. In Refs. 19 and 20, however, the region of interest is only the parabolic trajectory corresponding to the footprint of a fixed target at the SAR image plane, rather than the whole 2-D image plane. In this sense, the processor is only 1-D, not 2-D. Moreover, the unwanted part of the radar signal does not include the clutter scattered from the environment. It only consists of the white Gaussian noise.

Exploiting the multiresolution characteristics in SAR imagery using a physics-based approach seems promising. The mathematical formulation of the radar-return signal and chirp-compression processor in Refs. 21 and 22, together with a physical-optics model for the target scatterer, were used in Refs. 23 and 24 to provide a first-principles analysis for discerning specular returns from diffuse returns in synthetic aperture radar imagery by means of their distinct multiresolution patterns. Because the scattering pattern of a specular reflector is directional rather than isotropic, its resulting optimum processing duration is shorter than that of a conventional chirp-compression processor. This analysis verifies the empirical results from real SAR data that were reported in Ref. 14. However, the scenario considered in Refs. 23 and 24 is restricted to a simple case: 1-D, continuous-wave, nonpolarimetric, stripmap-mode imaging of a single reflector embedded in clutter. In addition, the target recognition in these cases is restricted to binary detection. To establish a comprehensive first-principles analysis for target detection and classification in SAR imagery, a significant amount of work remains to be done.

Motivated by the work of Refs. 23 and 24, we undertake a complete physics-based analysis of target detection and classification using SAR imagery. The operational conditions are extended to a more realistic case: 2-D, chirp-pulse waveform, and full polarimetric data collection. The radar scenarios of interest include stripmap-mode and spotlight-mode SARs. The targets consist of a repertoire of geometrically simple reflectors, including a specular mirror, a dihedral reflector, a trihedral reflector, and a tophat-shaped reflector. The point of choosing these reflector types is to deal with several fundamental wave-scattering mechanisms: single reflection (specular), directional double reflection (dihedral), triple reflection (trihedral), and nondirectional double reflection (tophat). The clutter is assumed to originate from a rough reflecting surface. Both the target and clutter returns are modeled from electromagnetic scattering theory.

The purpose of adopting electromagnetic theory is not to produce an accurate and comprehensive simulation of SAR images, but rather to provide a fundamental signal-model understanding for optimizing certain SAR signal-processing schemes. Our goal is neither to develop a specific target-recognition algorithm, nor to evaluate empirically such an algorithm by processing the real SAR data and comparing the results with those from other algorithms. Instead, we intend to study the performance of a generic target-recognition approach from a theoretical, model-based perspective. Specifically, we aim to answer the following questions. Under our assumed signal, clutter, and noise models, how much gain does the optimum likelihood-ratio target recognizer have over the likelihood-ratio recognizer based on a conventional SAR image processor? How much of this gain is due to the adaptive-resolution arrangement, polarimetric arrangement, or whitening of the clutter spectrum in the optimum processor? And is it plausible to approximate the complicated optimum recognizer with a simpler scheme under some circumstances? Although we have not translated our generic scheme of an optimum likelihood-ratio recognizer into an actual SAR ATR algorithm sophisticated enough to handle data in the real world (and henceforth do not compare the results of our performance analysis with the performances of other SAR ATRs), the answers to the previous questions shed light on implementing this algorithm as well as on understanding the effects of different features in this algorithm.

The remainder of this work is organized as follows. Section 2 describes the signal and processor models for the stripmap-mode and spotlight-mode SARs. The signal of concern includes three components: target return, clutter, and noise. The types of processors are conventional, adaptive-resolution, and Neyman-Pearson optimum. Section 3 presents performance results for multicomponent target detection. We compare the numerical values of these results, namely receiver operating characteristics, for different processors and target scenarios. Targets constituting only a few number (three) of reflectors are chosen to study the effects of simple reflectors' features on the likelihood-ratio-based processors. Sections 4 and 5 develop optimum likelihood-ratio classifiers for multicomponent targets with known and unknown positions, and present the numerical results of their performances, namely the probabilities of correct classification, in comparison with those from the

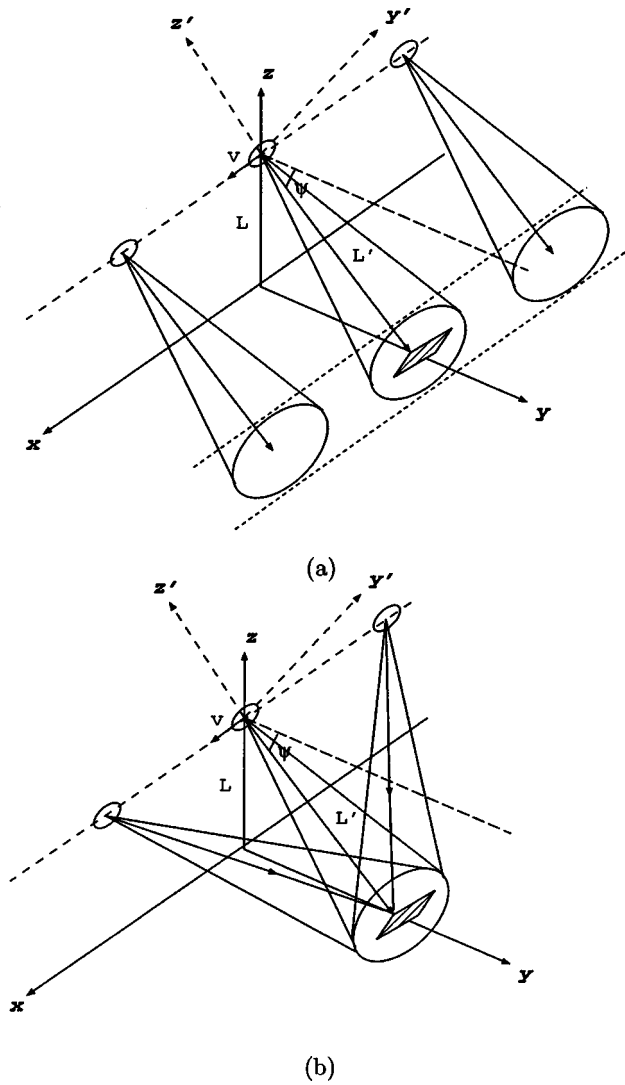


Fig. 1 Flight geometry for a 2-D SAR: upper panel is the stripmap mode, and the lower panel is the spotlight mode.

classifiers based on the conventional SAR processors. A more complex target scenario that has closer resemblance to a realistic condition is considered: four distinct targets comprising nine to ten reflector components. The probability of correct classification for this complex target scenario is difficult to compute. Instead, we develop upper and lower bounds and present Monte Carlo simulation results for this probability. Section 6 is a brief conclusion.

2 2-D SAR Signal and Processor Models

The stripmap and spotlight SAR modes we consider are sketched in Fig. 1. The radar is mounted on an aircraft flying with velocity $\vec{v} = \hat{x}v$ at an altitude of L m, hence its position at time t is given by the vector $\vec{r}_t = \hat{x}vt + \hat{z}L$. The direction $-\hat{z}' = -\hat{z} \sin(\psi) + \hat{y} \cos(\psi)$ in Fig. 1 is on the plane perpendicular to the velocity vector \vec{v} and tilted downward from the horizontal direction \hat{y} with angle ψ , making $L' = L/\sin(\psi)$ the range to the ground. The radar transmits a sequence of pulses toward the region of interest on the ground. The time-domain structure of this 2-D con-

figuration consists of a dimensionless discrete coordinate m along the cross-range direction, which is the pulse-number index, and a continuous-time coordinate τ along the range direction, corresponding to the time delay of the radar return.²⁴ The only difference between stripmap- and spotlight-mode operations is the normal direction of antenna aperture. In stripmap-mode operation, this normal is fixed at $-\hat{z}'$, so that as the aircraft flies, the antenna-beam footprint sweeps out an elongated strip on the ground at distance $L/\tan(\psi)$ from the projection of aircraft trajectory and with width $\lambda_c L/d \sin(\psi)$, where d is the radar's antenna diameter and λ_c is its wavelength. In spotlight-mode operation, however, the antenna's normal direction is adjusted along the flight path to constantly point toward the region centered at $(x, y, z) = [0, L \cot(\psi), 0]$, so that it "spotlights" a fixed footprint region of width $\lambda_c L/d \sin(\psi)$.

In both the stripmap- and spotlight-mode scenarios, the radar emits a train of modulated pulses which then propagate to the target region, where they are scattered (reflected) by the object and then propagate back to the receiving antenna. The waveform collected by the receiver is therefore a superposition of target return, clutter, and receiver noise. Because we are mainly interested in discriminating manmade objects from natural backgrounds, we consider the target return to have come from a geometrically simple reflector or reflectors, and the clutter from a random rough reflecting surface. Both are treated via electromagnetic theory.

2.1 Radar Return Models

We assume that the transmitter radiates a repetitive train of pulses with period T_s , complex envelope $p(t)$, and carrier angular frequency Ω_c s⁻¹ from an aperture S_a . The resulting electric field on the surface of this aperture is

$$\vec{E}_a(\vec{r}_a, t) = \text{Re} \left[\hat{u}_a (\eta P_T)^{1/2} U_{\text{ant}}(\vec{r}_a) \sum_{m=-\infty}^{\infty} p(t - mT_s) \times \exp(-i\Omega_c t) \right], \quad (1)$$

where \vec{r}_a is the spatial coordinate vector within S_a in the radar's rest frame, \hat{u}_a represents the polarization of the transmitted field \vec{E}_a , P_T is the peak transmitter power, $\eta = (\mu_0/\epsilon_0)^{1/2}$ is the natural impedance of free space, and $U_{\text{ant}}(\vec{r}_a)$ is the stationary spatial antenna aperture pattern in the radar's rest frame. We use an elliptical-Gaussian spatial pattern to model the finite aperture dimensions of the transmitter antenna,²⁴

$$U_{\text{ant}}(\vec{r}_a) = \left(\frac{2}{\pi a_x a_y} \right)^{1/2} \exp[-(x_a/a_x)^2 - (y_a/a_y)^2], \quad (2)$$

where x_a is the coordinate in the along-track (cross-range) direction, y_a is the coordinate in the across-track (range) direction, and a_x and a_y are the radii of S_a associated with the along- and across-track directions, respectively. The complex envelope $p(t)$ is assumed to be a chirped Gaussian pulse with duration T_0 and chirp bandwidth W_0 :

$$p(t) = \exp[-i\pi W_0 t^2 / T_0 - 4(t/T_0)^2]. \quad (3)$$

The return of the incident radar wave from a target can be modeled via scattering theory. For an incident monochromatic plane wave with propagation direction \hat{k}_i , angular frequency Ω , and wave number $k = \Omega/c$, namely, $\bar{E}_i(\bar{r}, t) = \text{Re}\{\bar{E}_{i0} \exp[i(k\hat{k}_i \cdot \bar{r} - \Omega t)]\}$, the scattered wave in the far-field zone $kr \gg 1$ is²⁵

$$\bar{E}_s(\bar{r}, t) = \text{Re}\left[\frac{\exp(ikr)}{r} \bar{S}(\hat{r}, \hat{k}_i, \Omega) \cdot \bar{E}_{i0} \exp(-i\Omega t)\right]. \quad (4)$$

Here \bar{r} is in the local coordinate whose origin is at the object center, and $\bar{S}(\hat{r}, \hat{k}_i; \Omega)$ is the object's bistatic scattering tensor as a function of the incident direction \hat{k}_i , scattering direction $\hat{r} = \bar{r}/|\bar{r}|$, and (angular) frequency Ω . The transmitted radar pulse is a superposition of monochromatic plane waves. Therefore the field scattered from the target can be obtained by summing all the scattering fields corresponding to the individual monochromatic plane-wave components. The result is a superposition of spherical waves modulated by the scattering tensors.

The radar return is collected by the receiving antenna and is taken to have a phasor complex envelope $y(t)$, consisting of a train of return pulses separated by T_s s. Because the returns associated with two adjacent pulses are ordinarily nonoverlapping, we can extract from $y(t)$ a 2-D signal $r(m, \tau)$, in which the discrete index m represents the pulse number, and the continuous time τ spans the interval $(-T_s/2, T_s/2)$:

$$y(t) \approx \sum_{m=-\infty}^{\infty} r(m, t - mT_s - 2L'/c). \quad (5)$$

The polarimetric signature that is embedded in the scattering function can be exploited by choosing different incident (\hat{u}_a) and receiving (\hat{u}_c) polarizations. In what follows, we define the aircraft flight direction \hat{x} to be vertical polarization, and the direction \hat{y}' , which is orthogonal to \hat{x} and the antenna's nominal direction \hat{z}' , to be horizontal polarization. In all cases we consider the HH , VV , and HV components of the radar return; VH , being identical to HV because of reciprocity, will not be explicitly treated. We use the boldface symbol to denote the fully polarimetric return signal, namely,

$$\mathbf{r}(m, \tau) = \begin{bmatrix} r_{HH}(m, \tau) \\ r_{VV}(m, \tau) \\ r_{HV}(m, \tau) \end{bmatrix}. \quad (6)$$

By means of the Fraunhofer approximation, we can derive the 2-D complex polarimetric target return from Eqs. (1) through (6). It can be shown that for a simple scatterer located at $(x, y, z) = [\Delta_x, \Delta_y + L' \cot(\psi), 0]$ away from the scene center $(x, y, z) = [0, L' \cos(\psi), 0]$, the 2-D complex polarimetric target return associated with stripmap-mode operation is²⁶:

$$\begin{aligned} \mathbf{r}_{\text{target}}(m, \tau) &\approx - \int_{-\infty}^{\infty} \frac{d\Omega}{2\pi} P(\Omega) \exp\{-i\Omega[\tau - 2\Delta_y \cos(\psi)/c]\} \\ &\times \mu_0^2(\Omega_c + \Omega)^2 \frac{\sqrt{P_T} a_x a_y}{4\pi \eta L'^2} \exp(i2k_c\{L' + \Delta_y \cos(\psi) \\ &+ [\Delta_y \sin(\psi)]^2/2L'\}) \exp[ik_c(mvT_s - \Delta_x)^2/L'] \\ &\times \exp\{-[(k_c + k)a_x(mvT_s - \Delta_x)]^2/2L'^2\} \\ &\times \exp\{-[(k_c + k)a_y \Delta_y \sin(\psi)]^2/2L'^2\} \\ &\times \mathbf{U}_c \cdot \bar{S}' \left(\frac{\hat{z}'L' + \hat{x}mvT_s/L' - \hat{x}\Delta_x - \hat{y}\Delta_y}{|\hat{z}'L' + \hat{x}mvT_s/L' - \hat{x}\Delta_x - \hat{y}\Delta_y|}, \right. \\ &\left. \frac{-\hat{z}'L' - \hat{x}mvT_s/L' - \hat{x}\Delta_x - \hat{y}\Delta_y}{|\hat{z}'L' + \hat{x}mvT_s/L' - \hat{x}\Delta_x - \hat{y}\Delta_y|}, \Omega_c + \Omega \right) \cdot \mathbf{U}_a, \quad (7) \end{aligned}$$

and the 2-D complex polarimetric target return associated with spotlight-mode operation is²⁶:

$$\begin{aligned} \mathbf{r}_{\text{target}}(m, \tau) &\approx - \int_{-\infty}^{\infty} \frac{d\Omega}{2\pi} P(\Omega) \exp\{-i\Omega[\tau - 2\Delta_y \cos(\psi)/c]\} \\ &\times \mu_0^2(\Omega_c + \Omega)^2 \frac{\sqrt{P_T} a_x a_y}{4\pi \eta L'^2} \exp(i2k_c\{L' + \Delta_y \cos(\psi) \\ &+ [\Delta_y \sin(\psi)]^2/2L'\}) \exp[ik_c(mvT_s - \Delta_x)^2/L'] \\ &\times \exp\{-[(k_c + k)a_x \Delta_x]^2/2L'^2\} \\ &\times \exp\{-[(k_c + k)a_y \Delta_y \sin(\psi)]^2/2L'^2\} \\ &\times \mathbf{U}_c \cdot \bar{S}' \left(\frac{\hat{z}'L' + \hat{x}mvT_s/L' - \hat{x}\Delta_x - \hat{y}\Delta_y}{|\hat{z}'L' + \hat{x}mvT_s/L' - \hat{x}\Delta_x - \hat{y}\Delta_y|}, \right. \\ &\left. \frac{-\hat{z}'L' - \hat{x}mvT_s/L' - \hat{x}\Delta_x - \hat{y}\Delta_y}{|\hat{z}'L' + \hat{x}mvT_s/L' - \hat{x}\Delta_x - \hat{y}\Delta_y|}, \Omega_c + \Omega \right) \cdot \mathbf{U}_a. \quad (8) \end{aligned}$$

In Eqs. (7) and (8),

$$\mathbf{U}_a = \begin{bmatrix} \hat{u}_H \\ \hat{u}_V \\ \hat{u}_H \end{bmatrix}; \quad \mathbf{U}_c = \begin{bmatrix} \hat{u}_H \\ \hat{u}_V \\ \hat{u}_V \end{bmatrix} \quad (9)$$

are the transmitter and receiver polarization tensors, respectively, and the modified scattering tensor \bar{S}' is related to the scattering tensor \bar{S} defined in Eq. (4) as follows,

$$\begin{aligned} &\frac{i(\Omega_c + \Omega)\mu_0}{4\pi} (\bar{I} - \hat{r}_s \hat{r}_s) \cdot \bar{S}'(\hat{r}_s, \hat{r}_i, \Omega_c + \Omega) \\ &= \bar{S}(\hat{r}_s, \hat{r}_i, \Omega_c + \Omega), \quad (10) \end{aligned}$$

where $\hat{r}_s \approx -\hat{r}_i$ is the unit direction connecting the scatterer center to the antenna aperture center. Notice that the only difference between Eqs. (7) and (8) is the cross-range an-

tenna beam pattern, $\exp\{-(k_c+k)a_x(mvT_s-\Delta_x)^2/2L'^2\}$ for the stripmap mode, and $\exp\{-(k_c+k)a_x\Delta_x^2/2L'^2\}$ for the spotlight mode.

The target types considered in this work include a specular, dihedral, trihedral, and tophat reflector. The specular reflector we model is a square flat plate with sides of length $2\rho_t$ and a perfectly conducting surface. Its bistatic scattering tensor can be calculated from physical optics. The dihedral reflector we consider consists of two perfectly conducting rectangular plates 1 and 2, whose edges meet at a right angle. The two plates are squares with sides of length $\sqrt{2}\rho_t$. The orientation of this dihedral is defined by two unit vectors: the dihedral axis \hat{n}_{axis} is the intersecting edge of the two plates, and the normal axis \hat{n}_{face} is perpendicular to \hat{n}_{axis} and bisects the 90-deg angle formed by the two plates. Four terms in the reflected field from this dihedral are significant: specular reflection from plate 1 to the radar; specular reflection from plate 1 to plate 2 to the radar; double reflection from plate 1 to plate 2 to the radar; and double reflection from plate 2 to plate 1 to the radar. To calculate these terms, we parallel the approach in Ref. 27. The two single-reflection terms are obtained as was done in the specular reflector case. The two double-reflection terms are obtained by using geometric optics to calculate the reflection from the first plate to the second, which is then used as the incident wave for calculating the double-reflection contribution to the radar return via the physical-optics approximation. The analytic expressions for the scattering tensors of a specular and a dihedral reflector are given in Ref. 26.

The trihedral reflector consists of three perfectly conducting rectangular plates 1, 2, and 3, whose edges meet at right angles. The three plates are squares with sides of length $\sqrt{2}\rho_t$. Each pair of plates intersect at an edge. The three intersecting edges form a rectangular coordinate system $(\hat{x}_b, \hat{y}_b, \hat{z}_b)$. Hence the orientation of the trihedral reflector can be defined by the spatial relation between the trihedral coordinate system $(\hat{x}_b, \hat{y}_b, \hat{z}_b)$ and the original coordinate system $(\hat{x}, \hat{y}, \hat{z})$. In the default orientation, the trihedral sits on top of the ground and faces the radar location at $m=0$, so that \hat{z}_b is identical to \hat{z} and $\hat{y} = (\hat{x}_b + \hat{y}_b)/\sqrt{2}$. In general, the trihedral reflector can rotate around the \hat{z}_b , the $(\hat{x}_b + \hat{y}_b)/\sqrt{2}$, or the $(-\hat{x}_b + \hat{y}_b)/\sqrt{2}$ axis. In most literature on radar target recognition, the trihedral reflector is modeled as a point scatterer with an isotropic scattering pattern. We adopt a more electromagnetics-based approach to calculate its scattering coefficient. Similar to the case of dihedral, we compute the distinct physical-optics terms of the radar return corresponding to the rays with different bounces. They are specular reflections from plates 1, 2, and 3; double reflections via the paths of plate 1 to 2, 1 to 3, 2 to 1, 2 to 3, 3 to 1, and 3 to 2; and triple reflections via the paths of plate 1 to 2 to 3, 1 to 3 to 2, 2 to 1 to 3, 2 to 3 to 1, 3 to 1 to 2, and 3 to 2 to 1. Except for a very limited spatial regime, the triple reflection terms dominate the double- and specular-reflection terms. To obtain a triple-reflection term of the scattering field, we use geometric optics to calculate the reflection from the first plate to the second, and the second to the third, which is then used as the incident wave for calculating the triple-reflection contribution to the radar return via the physical-optics approximation. This method parallels the one used in dihedral cal-

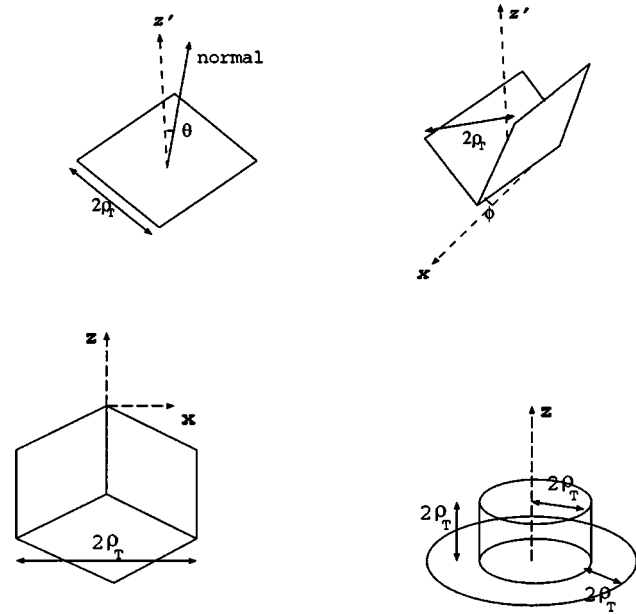


Fig. 2 Reflector types. Upper left: specular; upper right: dihedral; lower left: trihedral; lower right: tophat.

ulation. Compared with the simple assumption of a point scatterer, the electromagnetics-based approach is able to characterize the broad but nonisotropic spatial scattering pattern of a trihedral reflector.

The tophat reflector consists of a perfectly conducting cylinder sitting on top of a circular perfectly conducting plate; the overall shape is that of a tophat. The radius and the height of the cylinder are both $2\rho_t$, while the radius of the circular plate is $4\rho_t$. We assume the bottom of the tophat is located on the ground. The entire reflector, including the circular plate and the cylinder, is symmetric to the \hat{z} axis. Unlike the case of trihedral or dihedral, there is no need to specify the orientation of a tophat. The scattered field from a tophat reflector consists of five terms: the specular reflections from the top plate, the side of the cylinder, the bottom plate, and the double reflections via the paths of the bottom plate to the cylinder, and of the cylinder to the bottom plate. Like a dihedral, a tophat has most of its scattered field coming from the double-reflection terms. But different from a dihedral, the double reflections from a tophat are strong for all incident directions due to the symmetric geometry of the cylinder. To obtain a double-reflection term of the scattering field, we use geometric optics to calculate the reflection from the bottom plate to the cylinder, or the cylinder to the bottom plate, and then use this geometric-optics field as the incident wave for calculating the double-reflection contribution from the cylinder or the bottom plate via the physical-optics approximation.

The specular, dihedral, trihedral, and tophat reflectors embody different types of scattering mechanisms. The radar return from a specular reflector is a single bounce; the return from a dihedral or a tophat is mostly double bounces; while the return from a trihedral is dominated by triple-bounce terms. The distinction in terms of the number of bounces makes significant differences in the polarimetric patterns of these reflectors' radar returns. Figure 2 illus-

trates the four reflector types.

In addition to the target return we have just modeled, we need a physics-based approach for treating clutter. Clutter typically refers to the radar return from anything other than the desired target. In this study, clutter is assumed to be reflection from an infinite-extent rough ground surface. To calculate the clutter return, we apply a backpropagation formulation²¹ and the Kirchhoff approximation.²⁸ The resultant analytical expression for clutter return is in the form of a 2-D integral over the ground plane $x_b - y_b$ ²⁶:

$$\begin{aligned} \mathbf{r}_{\text{clutter}}(m, \tau) \approx & -\frac{\sqrt{P_T}\Omega_c^2 a_x a_y}{2\pi c^2 L'^2} \exp(i2k_c L') \\ & \times \sin(\psi) \int_{-\infty}^{\infty} \int_{-\infty}^{\infty} dx_b dy_b \\ & \times p[\tau - 2y_b \cos(\psi)/c] \\ & \times \exp[(ik_c/L' - k_c^2 a_x^2/2L'^2)(x_b - mvT_s)^2] \\ & \times \exp[(ik_c/L' - k_c^2 a_y^2/2L'^2)y_b^2 \sin^2(\psi)] \\ & \times \exp\{i2k_c[y_b \cos(\psi) + h(x_b, y_b)\sin(\psi)]\} \\ & \times \begin{bmatrix} R_{HH}(x_b, y_b) \\ R_{VV}(x_b, y_b) \\ R_{HV}(x_b, y_b) \end{bmatrix}, \end{aligned} \quad (11)$$

for stripmap-mode operation, and

$$\begin{aligned} \mathbf{r}_{\text{clutter}}(m, \tau) \approx & -\frac{\sqrt{P_T}\Omega_c^2 a_x a_y}{2\pi c^2 L'^2} \exp(i2k_c L') \\ & \times \sin(\psi) \int_{-\infty}^{\infty} \int_{-\infty}^{\infty} dx_b dy_b \\ & \times p[\tau - 2y_b \cos(\psi)/c] \end{aligned}$$

$$\begin{aligned} & \times \exp[ik_c/L'(x_b - mvT_s)^2] \\ & \times \exp[-(k_c^2 a_x^2/2L'^2)x_b^2] \\ & \times \exp[(ik_c/L' - k_c^2 a_y^2/2L'^2)y_b^2 \sin^2(\psi)] \\ & \times \exp\{i2k_c[y_b \cos(\psi) + h(x_b, y_b)\sin(\psi)]\} \\ & \times \begin{bmatrix} R_{HH}(x_b, y_b) \\ R_{VV}(x_b, y_b) \\ R_{HV}(x_b, y_b) \end{bmatrix}, \end{aligned} \quad (12)$$

for spotlight-mode operation. In these expressions, $h(x_b, y_b)$ is the surface height at (x_b, y_b) , R_{HH} , R_{VV} , and R_{HV} are the HH , VV , and HV components of the dyadic reflection tensor \bar{R} . The clutter in Eqs. (11) or (12) can be interpreted as the sum of contributions from all points on the ground plane, whose scattering coefficients are proportional to the local reflectivities.

We model $h(x_b, y_b)$, $R_{HH}(x_b, y_b)$, $R_{VV}(x_b, y_b)$, and $R_{HV}(x_b, y_b)$ in Eqs. (11) and (12) as stochastic processes. Paralleling the work in Refs. 21 and 22, we define a field transition coefficient:

$$\mathbf{T}(x_b, y_b) = \exp[i2k_c h(x_b, y_b)\sin(\psi)] \begin{bmatrix} R_{HH}(x_b, y_b) \\ R_{VV}(x_b, y_b) \\ R_{HV}(x_b, y_b) \end{bmatrix}. \quad (13)$$

Assuming that $\sqrt{\langle h^2 \rangle} \gg \lambda_c$, and that the reflection coefficients $R_{\alpha\beta}$ are independent of the surface height profile h , we can take \mathbf{T} to be a zero-mean, circulo-complex, white, vector Gaussian random process, fully characterized by

$$\begin{aligned} \langle \mathbf{T}(x_b, y_b) \mathbf{T}^\dagger(x'_b, y'_b) \rangle &= \frac{\lambda_c^2}{\sin^2(\psi)} \delta(x_b - x'_b) \delta(y_b - y'_b) \\ & \times \begin{bmatrix} \langle |R_{HH}(x_b, y_b)|^2 \rangle & \langle R_{HH}(x_b, y_b) R_{VV}^*(x_b, y_b) \rangle & \langle R_{HH}(x_b, y_b) R_{HV}^*(x_b, y_b) \rangle \\ \langle R_{HH}^*(x_b, y_b) R_{VV}(x_b, y_b) \rangle & \langle |R_{VV}(x_b, y_b)|^2 \rangle & \langle R_{HV}^*(x_b, y_b) R_{VV}(x_b, y_b) \rangle \\ \langle R_{HH}^*(x_b, y_b) R_{HV}(x_b, y_b) \rangle & \langle R_{VV}^*(x_b, y_b) R_{HV}(x_b, y_b) \rangle & \langle |R_{HV}(x_b, y_b)|^2 \rangle \end{bmatrix}. \end{aligned} \quad (14)$$

Note that the correlation matrix in Eq. (14) includes the polarimetric behavior of the clutter return, which can depend significantly on the geographic region under inspection. We assume there is a statistically uniform terrain texture within the radar footprint. Therefore the correlation matrix in Eq. (14) is approximately independent of x_b and y_b . Empirical work⁷ suggests

that: all the off-diagonal components in Eq. (14) are insignificant except for the $HH \times VV$ terms; the $HH \times HH$ and $VV \times VV$ terms are approximately equal; and the strength of $HV \times HV$ term is significantly smaller than that of the $HH \times HH$ term, unless multiple scattering is prominent. Thus, in our radar clutter model, we use

$$\langle \mathbf{T}(x_b, y_b) \mathbf{T}^\dagger(x'_b, y'_b) \rangle = \frac{\lambda_c^2}{\sin^2(\psi)} \delta(x_b - x'_b) \delta(y_b - y'_b) \times \begin{bmatrix} 1 & \rho & 0 \\ \rho^* & 1 & 0 \\ 0 & 0 & \epsilon \end{bmatrix}, \quad (15)$$

where $0 < |\rho| < 1$ and $0 < \epsilon < 1$.

The final element in our radar signal model is receiver noise. Typically, this is thermal noise, and has a white spectrum. In this work, for both stripmap- and spotlight-mode operations, the receiver noise $\mathbf{r}_{\text{noise}}(m, \tau)$ is assumed to be a zero-mean, circulo-complex, vector Gaussian stochastic process that is white in all its domains, namely its discrete-time index m , its continuous-time parameter τ , and its vector (polarimetric) domain. Thus it is completely characterized by the following correlation matrix,

$$\langle \mathbf{r}_{\text{noise}}(m, \tau) \mathbf{r}_{\text{noise}}^\dagger(m', \tau') \rangle = N_0 \delta[m - m'] \delta(\tau - \tau') \times \begin{bmatrix} 1 & 0 & 0 \\ 0 & 1 & 0 \\ 0 & 0 & 1 \end{bmatrix}. \quad (16)$$

Both of the unwanted components of the radar return, the clutter, and the noise are stochastic in our model. Because they have completely different physical origins, we assume that they are statistically independent of each other.

2.2 SAR Processor Models

In this work, two types of SAR image processing systems are considered: an adaptive-resolution processor and a whitening-filter processor. An adaptive-resolution processor is a conventional SAR processor with adjustable processing durations. In stripmap-mode operation, the incoming radar return is passed through chirp compression filters in both the cross-range (discrete-time) and range (continuous-time) domains. The output from these chirp compression filters is then video detected to form a radar intensity image. The impulse responses for the chirp compression filters are

$$h_1[m] = \exp[(-ik_c/L' - k_c^2 a_x^2 \kappa^2 / 2L'^2)(mvT_s)^2] \quad \text{and} \quad (17)$$

$$h_2(\tau) = \exp[(i\pi W_0/T_0 - 4/T_0^2)\tau^2].$$

When the resolution parameter $\kappa=1$, $h_1[m]$ is the complex conjugate of the cross-range-dependent factor in the radar return from a point scatterer. Similarly, $h_2(\tau)$ is the complex conjugate of the range-dependent factor in the radar return from a point scatterer. The point-scatterer radar return is obtained by carrying out the integral in Eq. (8) under the assumption that 1. $\Delta_x = \Delta_y = 0$, 2. $\Omega_c \gg \Omega$ within the bandwidth, and 3. the scattering tensor \bar{S}' of a point scatterer is the identity tensor \bar{I}' . A conventional 2-D stripmap SAR processor uses chirp compression filters $h_1[m]$ and $h_2(\tau)$ arranged (by setting $\kappa=1$) to be matched filters for the radar return from a point scatterer. An extended target

can have a very different return duration than that of a point scatterer. Thus our adaptive-resolution processor will be optimized over κ to achieve the best detection performance for such an extended target.

In spotlight-mode operation, a standard interpretation of the radar return is to conceive it as a convolved form of the 2-D Fourier transform of the terrain reflectivity profile, namely the tomographic rendition of the terrain reflectivity distribution.^{16,29} An adaptive-resolution spotlight-mode SAR processor²⁹ first dechirps the radar-return signal along the range and cross-range directions. The dechirped signal, which is still continuous for the range time, is sampled to become a 2-D discrete-time signal. The sampled signal, after rearrangement by a polar formatter, then undergoes a 2-D discrete Fourier transform operation. In this processor, the cross-range processing duration, which is the angular width of the polar-format annular region, and the range processing duration, which is the radial width of the polar-format annular region, are variables. To be specific, let the cross-range index m of the discrete dechirped signal chosen for further processing be from $-m_a/2$ to $m_a/2$, and let the range index n for further processing be from $-n_a/2$ to $n_a/2$. Thus m_a and n_a represent the cross-range and range processing durations, respectively. To be consistent with the notation in Eq. (17), we define

$$m_a \equiv \frac{2\sqrt{2}L'}{\kappa k_c a_x v T_s}, \quad n_a \equiv \frac{T_0}{T_r}. \quad (18)$$

Thus for the same κ , the processing durations of the adaptive-resolution stripmap-mode SAR and the spotlight-mode SAR processors are identical. The case $\kappa=1$ corresponds to the conventional spotlight-mode SAR processor.

Whereas the adaptive-resolution schemes just described can enhance SAR image resolution, they do not, in general, represent optimum receivers for binary detection of a deterministic target return embedded in stochastic clutter and noise. The optimum Neyman-Pearson processing scheme for a stripmap-mode SAR signal uses a filter to whiten the clutter plus noise, followed by a matched filter corresponding to the target-return waveform passed through the whitening filter, followed in turn by video detection, sampling, and a threshold test. The form of the whitening filter is determined by the covariance function of the clutter-plus-noise component of the radar return. The architecture of a spotlight-mode whitening processor is essentially the same as that for the stripmap-mode whitening processor. The only differences being that the spotlight-mode whitening processor must use time-shift compensation in its front end, and, of course, different impulse responses for its whitening and matched filters.

The whitening-filter processor is conceptually important in that it is the Neyman-Pearson optimum processor for the target detection problem. As such, its receiver operating characteristic—its detection versus false-alarm probability behavior—bounds the performance of any realizable processor. By comparing the detection performance of an adaptive-resolution processor with that of a whitening processor, we can see how far the former's detection performance is from the ultimate theoretical limit. By comparing the detection performance of the optimized adaptive-

resolution processor with its conventional-processor ($\kappa=1$) limit, we can quantify the importance of treating extended targets differently from point scatterers.

3 Multicomponent Target Detection

Targets in real SAR campaigns, such as tanks, are composed of small reflectors. In this section, we deal with the detection problem of the targets with multiple reflector components.

A multicomponent target is a collection of simple reflectors located at different positions. The radar-return signal from a single reflector located at $(\Delta_x, \Delta_y, 0)$ with respect to the scene center can be obtained from Eqs. (7) (stripmap mode) or (8) (spotlight mode). Because we neglect multiple scattering between different reflectors, the radar-return signal from a multicomponent target is the sum of the contributions from all its individual scatterers. On the other hand, the clutter and noise components in the radar return are unaltered by the change of target.

The multicomponent target detection problem is a binary hypothesis test: determine whether a (known) multicomponent target is present or absent from the given radar image corrupted with clutter and noise. Complete information about the multicomponent target includes the geometric type, size, material constitution, orientation, and center location of each reflector, and the phase of the radar return from each reflector. An effective target detection scheme need not necessarily take all of these parameters as given. Indeed, it may not be feasible to simultaneously cope with variations of all of these parameters. In this section, we choose to investigate two cases: each target component has a random phase; and each target component has a random phase and a random position.

In keeping with the aim to quantify, from a fundamental principles viewpoint, the target-recognition performance advantage of polarimetric adaptive-resolution processors as compared to conventional SAR imagers, the multicomponent target models chosen for investigation here are not as complicated as a real-world object, such as a tank or truck.

3.1 Multicomponent Target Detection with Unknown Phases/Positions

The binary hypothesis testing problem for the 2-D radar return of an M -component target can be formulated as follows: the IF complex envelope of radar return is

$$\mathbf{r}(m, \tau) \approx \mathbf{r}_{\text{clutter}}(m, \tau) + \mathbf{r}_{\text{noise}}(m, \tau) \quad (19)$$

when the target is absent (hypothesis H_0), or it is

$$\begin{aligned} \mathbf{r}(m, \tau) \approx & \sum_{p=1}^M \exp(i\tilde{\phi}_p) \mathbf{r}_p(m - m_p, \tau - \tau_p) + \mathbf{r}_{\text{clutter}}(m, \tau) \\ & + \mathbf{r}_{\text{noise}}(m, \tau) \end{aligned} \quad (20)$$

when the target is present (hypothesis H_1). Here $\mathbf{r}_{\text{clutter}}(m, \tau)$ and $\mathbf{r}_{\text{noise}}(m, \tau)$ are clutter and noise complex envelopes, respectively, as modeled in Sec. 1. The phase $\tilde{\phi}_p$ represents the incoherence of the p 'th target component, and the 2-D time delay (m_p, τ_p) is proportional to the location of the p 'th target component (Δ_x^p, Δ_y^p) via the rela-

tion $(\Delta_x^p, \Delta_y^p) = [m_p v T_s, c \tau_p / 2 \cos(\psi)]$. We assume that the $\{\tilde{\phi}_p\}$ are independent and uniformly distributed on $[0, 2\pi)$. Two target-location conditions are considered: 1. the $\{(\Delta_x^p, \Delta_y^p)\}$ are known; and 2. the $\{(\Delta_x^p, \Delta_y^p)\}$ are independent random vectors that are uniformly distributed within given uncertainty areas.

Consider first the detection of a multicomponent target with random phases and known reflector locations. To accomplish the Neyman-Pearson optimum detection scheme, we first pass the radar return $\mathbf{r}(m, \tau)$ through the whitening filter, leading to a complex envelope after the whitening filter, satisfying:

$$\mathbf{s}(m, \tau) \approx \mathbf{w}(m, \tau) \quad (21)$$

when the target is absent (hypothesis H_0), and

$$\mathbf{s}(m, \tau) \approx \sum_{p=1}^M \exp(i\tilde{\phi}_p) \mathbf{s}_p(m - m_p, \tau - \tau_p) + \mathbf{w}(m, \tau) \quad (22)$$

when the target is present (hypothesis H_1). Here $\mathbf{w}(m, \tau)$ is the clutter-plus-noise after the whitening filter, which is white in m, τ , and polarimetric domains, and \mathbf{s}_p is the output of \mathbf{r}_p from the whitening filter. When the spatial separations between the individual target components are large enough, the following orthogonality condition will prevail:

$$\sum_{m=-\infty}^{\infty} \int_{-\infty}^{\infty} d\tau \mathbf{s}_p^\dagger(m - m_p, \tau - \tau_p) \cdot \mathbf{s}_q(m - m_q, \tau - \tau_q) \approx 0 \quad (23)$$

for $p \neq q$. The reason is that $\mathbf{s}_p(m - m_p, \tau - \tau_p)$ or $\mathbf{s}_q(m - m_q, \tau - \tau_q)$, the footprint of reflectors p or q , has nonvanishing values only within a finite area on the (m, τ) plane. Thus when the two reflectors have a large spatial separation, either $\mathbf{s}_p(m - m_p, \tau - \tau_p)$ or $\mathbf{s}_q(m - m_q, \tau - \tau_q)$ has to be zero at every point on the (m, τ) plane. Under the orthogonality condition, which we assume to be true in all that follows, the likelihood ratio for the binary hypothesis test in Eqs. (21) and (22) is²⁶

$$\begin{aligned} \Lambda(\mathbf{s}) &= \frac{P_{\mathbf{s}|H_1}(\mathbf{s}|H_1)}{P_{\mathbf{s}|H_0}(\mathbf{s}|H_0)} \\ &= \prod_{p=1}^M \exp \left[- \sum_{m=-\infty}^{\infty} \int_{-\infty}^{\infty} d\tau \mathbf{s}_p^\dagger(m, \tau) \cdot \mathbf{s}_p(m, \tau) \right] \\ &\quad \times I_0 \left[2 \left| \sum_{m=-\infty}^{\infty} \int_{-\infty}^{\infty} d\tau \mathbf{s}_p^\dagger(m - m_p, \tau - \tau_p) \cdot \mathbf{s}(m, \tau) \right| \right], \end{aligned} \quad (24)$$

where I_0 is the modified Bessel function of zero order:

$$I_0(x) \equiv \frac{1}{2\pi} \int_0^{2\pi} d\phi \exp(x \cos \phi).$$

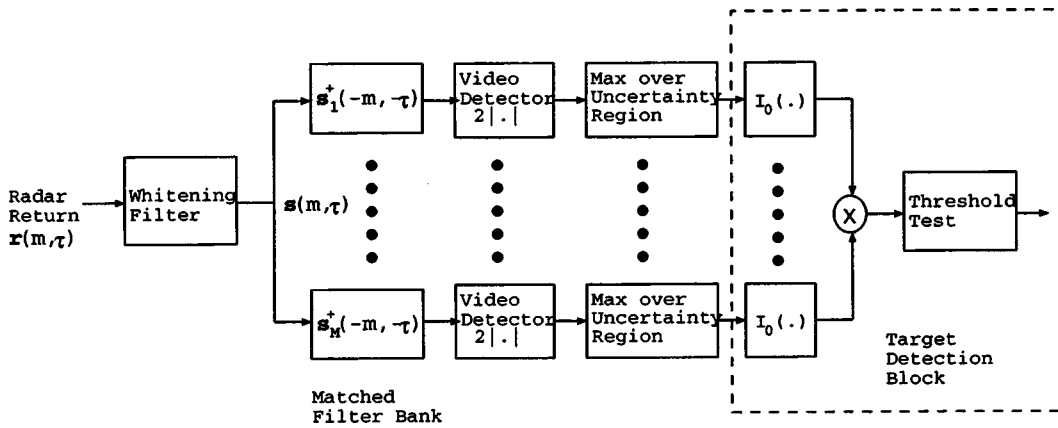


Fig. 3 GLR detector for the multicomponent target with unknown phases and positions.

The Neyman-Pearson optimum detection scheme for this binary hypothesis test is a threshold detector based on the likelihood ratio (LR), which can be simplified to

$$\prod_{p=1}^M I_0 \left[2 \left| \sum_{m=-\infty}^{\infty} \int_{-\infty}^{\infty} d\tau s_p^\dagger(m-m_p, \tau-\tau_p) \cdot s(m, \tau) \right| \right] \begin{matrix} \text{say } H_1 \\ > \\ < \\ \text{say } H_0 \end{matrix} \beta, \tag{25}$$

where the threshold β is chosen to meet the constraint on the false-alarm probability.

When, in addition to the phases $\{\tilde{\phi}_p\}$, the target-component delay times $\{(m_p, \tau_p)\}$ are also random variables, it becomes difficult to write down the likelihood ratio for the binary hypothesis testing problem. It is possible (and useful) to formulate the generalized likelihood ratio and develop a detector scheme on that basis.¹⁹ The generalized likelihood ratio is²⁶:

$$\Lambda(\mathbf{s}) = \max_{m_1, \dots, m_M, \tau_1, \dots, \tau_M} \left\{ \prod_{p=1}^M \exp \left[- \sum_{m=-\infty}^{\infty} \int_{-\infty}^{\infty} d\tau \times s_p^\dagger(m, \tau) \cdot s_p(m, \tau) \right] \times I_0 \left[2 \left| \sum_{m=-\infty}^{\infty} \int_{-\infty}^{\infty} d\tau s_p^\dagger(m-m_p, \tau-\tau_p) \cdot s(m, \tau) \right| \right] \right\}. \tag{26}$$

So the generalized-likelihood-ratio (GLR) detector based on Eq. (26) can be written in the following form:

$$\prod_{p=1}^M \max_{m_p, \tau_p} \left\{ I_0 \left[2 \left| \sum_{m=-\infty}^{\infty} \int_{-\infty}^{\infty} d\tau s_p^\dagger(m-m_p, \tau-\tau_p) \cdot s(m, \tau) \right| \right] \right\} \begin{matrix} \text{say } H_1 \\ > \\ < \\ \text{say } H_0 \end{matrix} \beta. \tag{27}$$

The GLR detector is basically an LR detector that uses maximum-likelihood estimates of the component delays as though they were the true reflector locations. The architecture of this GLR detector is sketched in Fig. 3.

Performance analysis for the GLR detector involves level crossing theory for a 2-D random field. Helstrom³⁰ provided a comprehensive treatment for the calculation of probabilities of detection and false alarm for a 1-D radar signal. He approximated the value of P_D from a GLR detector with the value of P_D from a LR detector with known position at a high signal-to-noise ratio. For P_F , he presented an analytical approach derived from the level crossing theory of a stationary 1-D random process, which is valid for small P_F when the uncertainty region for location exceeds the resolution length of the intensity profile after the matched filter. Shapiro et al.³¹ presented a finite-bin hypothesis-test approach for calculating P_D and P_F of a 1-D radar return. Based on these works, we developed formulations for evaluating the probabilities of detection and false alarm of the 2-D GLR detector. The details can be found in Ref. 26. We only present some numerical examples.

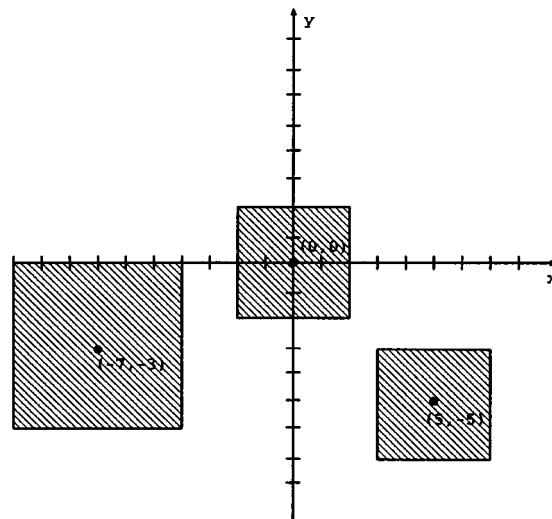
Suppose that the target of concern consists of three identical square specular reflectors at different locations. For all target components, the half length of each square reflector plate, ρ_t , is 0.5 m, and the plate's normal direction is \hat{z}' . The chirp bandwidth $W_0 = 200$ MHz, the clutter-to-noise ratio $\text{CNR} = 4.283 \times 10^{-3}$ (noise dominant), and all the remaining parameter values are the same as those in Table 1. For the target with known positions, the center locations of

Table 1 Table of parameter values for SNCR calculations.

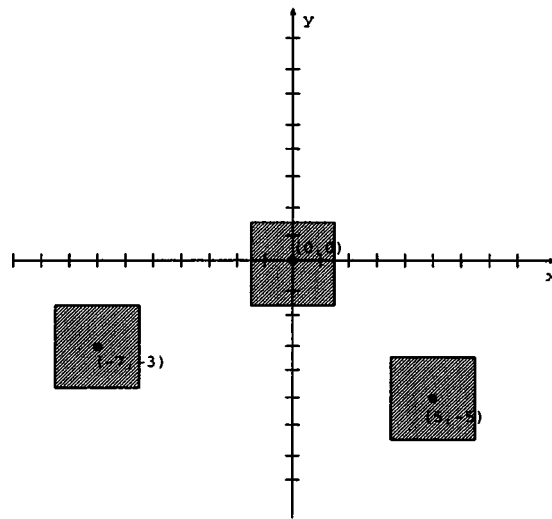
Flight parameters	Radar parameters	Reflector parameters
aircraft altitude $L = 5000$ m	antenna radii $a_x = a_y = 1$ m	target radii $\rho_t = 1.5$ m
aircraft speed $u = 100$ m/s	Tx power $P_T = 1$ W	relative permittivity $\epsilon_r = 10 + i5$
slant angle $\psi = 45$ deg	radar frequency $f_c = \Omega_c / 2\pi = 10$ GHz	HV clutter strength $\epsilon = 0.2$
	pulse-repetition period $T_s = 10$ ms	HH×VV correlation $\rho = 0.57$
	pulse width $T_0 = 0.05$ μs	
	chirp bandwidth $W_0 = 200$ MHz	

the three reflectors with respect to scene center are $(\Delta_x, \Delta_y) = (0,0)$, $(-7,-3)$, and $(5,-5)$ (in units of meters). For the target with random positions, the center locations of the three reflectors are uniformly distributed within square uncertainty regions centered at $(0,0)$, $(-7,-3)$, and $(5,-5)$. Two sets of specifications for these uncertainty regions are considered. In the first set, the edge lengths of the square uncertainty regions for components 1, 2, and 3 are 4, 6, and 4 m, respectively. In the second set, the edge lengths of the square uncertainty regions for components 1, 2, and 3 are 3, 3, and 3 m, respectively. Figure 4 plots these two uncertainty specifications.

Figure 5 plots the receiver operating characteristics (ROCs) of the LR detectors for the example target with unknown positions. The figure includes both stripmap- and spotlight-mode results. There are three curves in each panel, corresponding to the behavior of the LR detector for the multicomponent target with no position uncertainty, with position uncertainty specification 1 in Fig. 4, and with position uncertainty specification 2 in Fig. 4. Note that the figure is plotted on probability-paper axes to permit accurate display of both high (near unity) and low (near zero) probability values. We first notice that, for the same target, spotlight-mode operation has better detection performance than does stripmap-mode operation. The reason is that the spotlight-mode target return has higher signal-to-noise-plus-clutter-ratio (SNCR) values than the stripmap-mode target return for all individual components. The physical reason behind this behavior is also clear: because spotlight-mode operation illuminates the target for a longer time duration than the stripmap-mode operation, its postfilter signal strengths are correspondingly higher. In addition, two phenomena in the numerical results in Fig. 5 are consistent with intuition: 1. when the precise information on the target components' locations is lost, the detection performance of the GLR detector is degraded; 2. the larger the uncertainty regions are, the greater this degradation becomes. Finally, we see that the ROC curves in Fig. 5 that correspond to the stripmap- and spotlight-mode operations have different slopes. This is a consequence of different target-return spectra (along the cross-range direction) between the two synthetic-aperture operating modes.



(a)



(b)

Fig. 4 Specifications for the uncertainty-region geometries. Upper panel: uncertainty specification 1. Lower panel: uncertainty specification 2. Notice that $(0,0)$ is the scene center of the antenna footprint area. The aircraft flies along the x direction.

3.2 Multicomponent Target Detection: Neyman-Pearson Processor Versus Conventional SAR Processor

The target detectors presented so far are Neyman-Pearson optimal, i.e., they optimally combine polarimetric, whitening-filter, and adaptive-resolution processing. As in our work on single-component target detection (presented in Ref. 26), the target detection performance of optimum multicomponent target processors must exceed that of conventional SAR processors for such targets. In this section, we explicitly compare the receiver operating characteristics

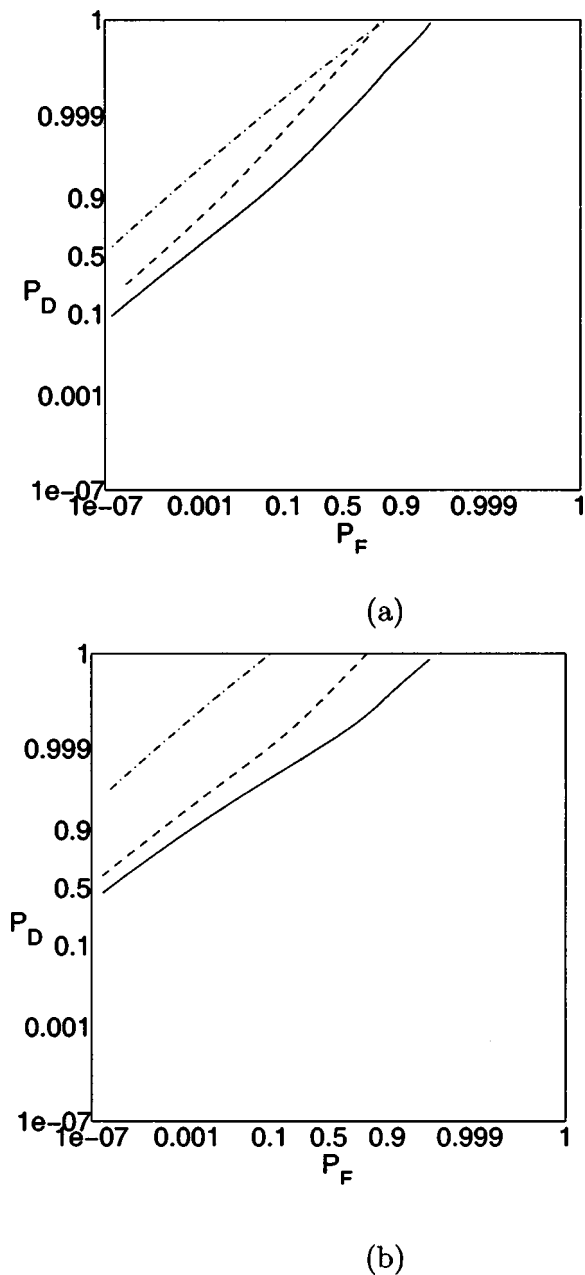


Fig. 5 Receiver operating characteristics. Three specular reflectors: likelihood-ratio detector for target with no position uncertainty (dashed dot curve); GLR detector for target with position uncertainty specification 1 (solid curve); and GLR detector for target with position uncertainty specification 2 (dashed curve). The upper panel is the stripmap-mode operation, and the lower panel is the spotlight-mode operation.

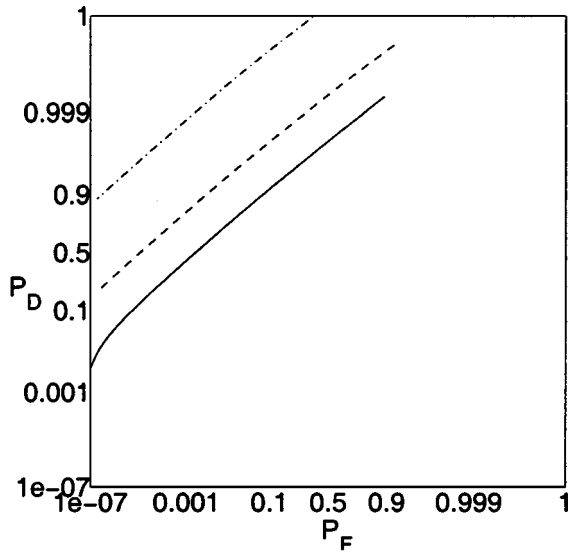
of the Neyman-Pearson processors with those of the conventional SAR processors to quantify the former's performance advantage.

The conventional SAR processors for a multicomponent target are straightforward extensions of the single-reflector versions that were described in Sec. 2. In contrast to the Neyman-Pearson processors that possess a bank of matched filters for the target's component reflectors, a conventional SAR processor has only one full-resolution ($\kappa=1$) chirp-compression SAR imager for stripmap-mode operation, or

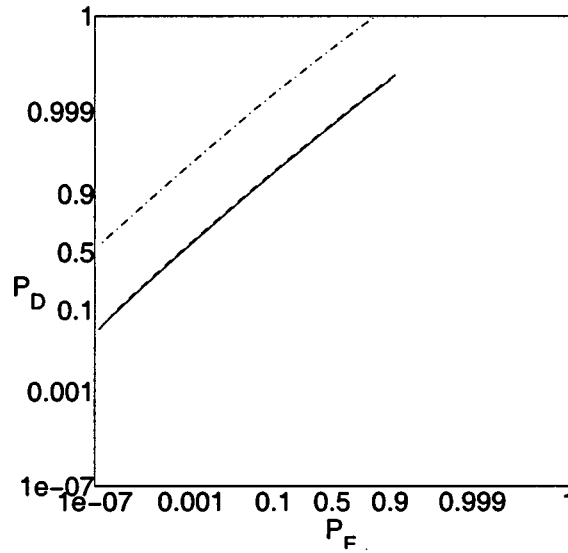
one full-resolution ($\kappa=1$) polar-format SAR imager for spotlight-mode operation. In addition, instead of the fully polarimetric signal dealt with in the Neyman-Pearson processor, only one single polarization is considered in the conventional SAR processor (here we choose HH). The target detectors after the SAR imager are similar to their counterparts in Neyman-Pearson processors: they sample this output image according to the available information on target-component locations and calculate the likelihood ratio or generalized likelihood ratio.

The receiver operating characteristics for these conventional SAR multicomponent target detectors can be calculated via techniques similar to those used for the Neyman-Pearson SAR processor.²⁶ Figure 6 compares the receiver operating characteristics of the conventional (full-resolution) SAR processor, the full-polarimetric Neyman-Pearson processor, and the scalar (single-polarized) adaptive-resolution processor when the target-component locations and radar-return amplitudes are exactly known. The target scenario is different from that specified in Fig. 5. In this case, the multicomponent target consists of three specular reflectors with $\rho_t=1.7$ m and the same known (Δ_x, Δ_y) positions as the one in Fig. 5. The clutter-to-noise ratio is set to be 8.56×10^{-4} . The other parameters are identical to those used in Fig. 5. Figure 7 also compares the receiver operating characteristics of these three processors when the target-component locations and radar-return amplitudes are exactly known, but with a different parameter set. In Fig. 7 all the parameter values are identical to those used in Fig. 5. Figure 8 is a comparison similar to Fig. 7 when the target-component locations are independently and uniformly random within 2-D uncertainty regions. It is clear in all cases from Figs. 6–8 that the Neyman-Pearson processor has a better detection performance than the conventional SAR processor. Thus the motivation for studying the polarimetric, whitening-filter, adaptive-resolution processor is verified: we have demonstrated from a first-principles approach that this kind of processor indeed outperforms the conventional full-resolution SAR processor in terms of not only single-component but also multicomponent target detection.

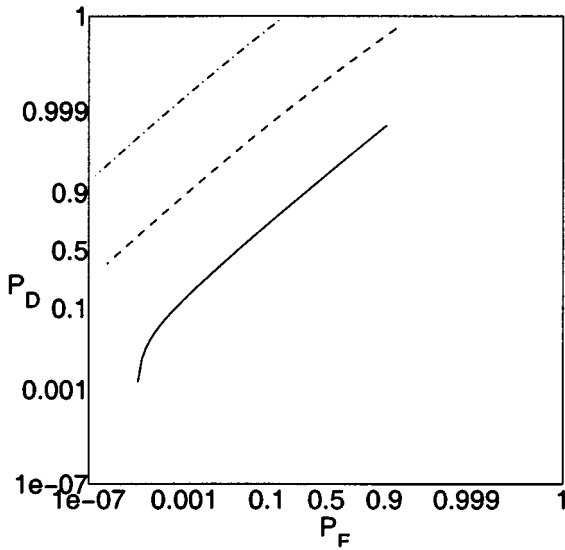
The superior target-detection performance of the Neyman-Pearson processors is the result of their having higher SNCR values for the target components. Three factors are responsible for this SNCR advantage: the effect of the whitening filter, the adaptive-resolution effect, and the polarimetric effect. In the multicomponent target examples we have considered so far, noise dominates over clutter. Thus the whitening filter does not have a major contribution. The adaptive-resolution effect can be very important when the size of the reflector is much larger (stripmap and spotlight mode) or smaller (spotlight mode) than the diameter of antenna aperture. The polarimetric effect in a Neyman-Pearson processor can enhance the SNCR value by a factor up to 2. In Fig. 6, the performance gap between the conventional SAR processor and adaptive-resolution processor and the gap between the adaptive-resolution processor and polarimetric Neyman-Pearson processor are both salient. Therefore, the performance improvement of the Neyman-Pearson processor due to adaptive-resolution processing is as significant as that due to polarimetric synthesis. In Figs. 7 and 8, the polarimetric effect is more



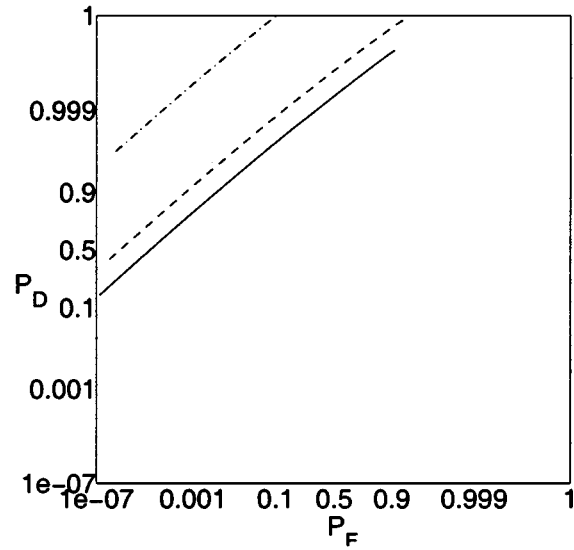
(a)



(a)



(b)



(b)

Fig. 6 Receiver operating characteristics: conventional SAR processor (solid curve) versus polarimetric (dashed dot curve) and non-polarimetric (dashed curve) Neyman-Pearson processors, multicomponent target with random phases, three specular reflectors with $\rho_t = 1.7$ m; and $\text{CNR} = 8.56 \times 10^{-4}$. (a) is the stripmap-mode operation, and (b) is the spotlight-mode operation.

Fig. 7 Receiver operating characteristics: conventional SAR processor (solid curve) versus polarimetric (dashed dot curve) and non-polarimetric (dashed curve) Neyman-Pearson processors, likelihood-ratio detector, multicomponent target with random phases, and three specular reflectors. (a) is the stripmap-mode operation, and (b) is the spotlight-mode operation.

salient than the adaptive-resolution effect because the chosen target size renders the full resolution close to the optimum resolution.²⁶

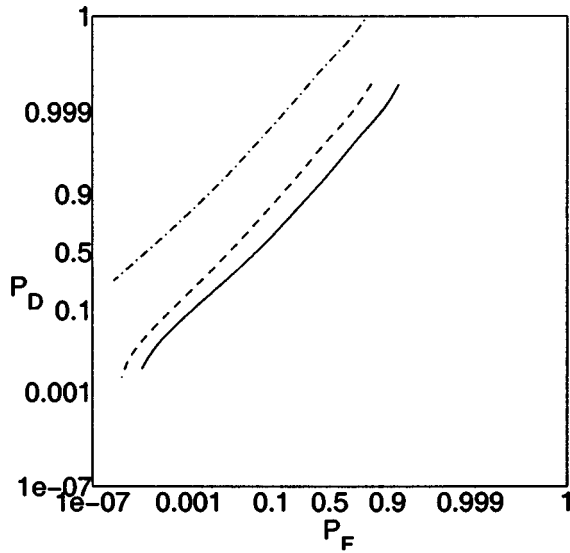
4 Multicomponent Target Classification with Known Reflector Positions

Target detection is binary target recognition: is a particular target present or not? A normal automatic target recognition system must deal with an N -ary problem: of $N \geq 2$ target types, which one (if any) is present, based on the radar-return information? This problem is also known as classi-

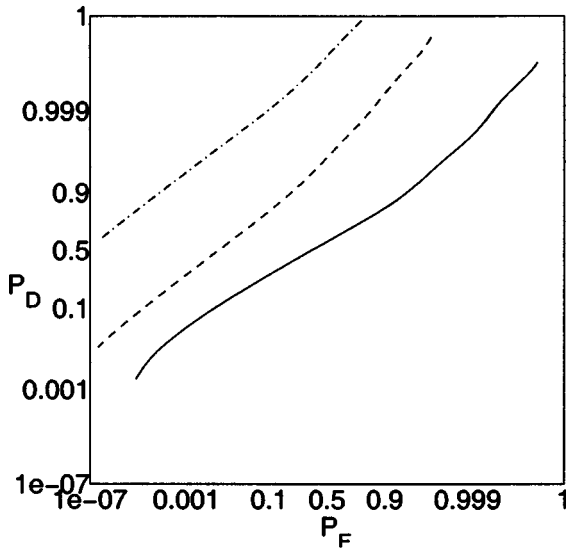
fication. In this section, we extend our previous results for target detection problems to multicomponent target classification problems with known reflector positions. We apply the Neyman-Pearson or conventional SAR target detectors we have already developed to form Neyman-Pearson or conventional SAR target classifiers. We also come up with a simple method for assessing the performance of these classifiers.

4.1 Classification Scheme

A multicomponent target classification problem is formulated in the following manner. Let $s(m, \tau)$ be the radar re-



(a)



(b)

Fig. 8 Receiver operating characteristics: conventional SAR processor (solid curve) versus polarimetric (dashed dot curve) and non-polarimetric (dashed curve) Neyman-Pearson processors, GLR detector, multicomponent target with random phases and position uncertainty specification 2, 3 specular reflectors. (a) is the stripmap-mode operation, and (b) is the spotlight-mode operation.

turn from a multicomponent target after passing through a whitening filter. Therefore, it has the unwanted clutter-plus-noise component whitened to unity spectral density. Then, following Eqs. (21) and (22), if H_i denotes that target i among all N possible targets is present, $s(m, \tau)$ can be written as follows:

$$\text{under } H_i: \quad s(m, \tau) = \sum_{p=1}^{M_i} \exp(i\tilde{\phi}_{p,i}) s_{p,i}(m - m_{p,i}, \tau - \tau_{p,i}) + \mathbf{w}(m, \tau) \quad \text{for } i = 1, \dots, N. \quad (28)$$

Here $\mathbf{w}(m, \tau)$ is the vector clutter-plus-noise complex envelope after the whitening filter. By construction it is white in the cross-range-time (m), the range-time (τ), and the polarimetric (vector) domains. Likewise, $s_{p,i}(m, \tau)$ corresponds to the postwhitening-filter radar-return complex envelope from the p 'th component of the i 'th target when the component is located at the scene center. The time delays $m_{p,i}$ and $\tau_{p,i}$ for this component are determined by its actual location. The phases $\{\tilde{\phi}_{p,i}\}$ are independent random variables that are uniformly distributed within $[0, 2\pi)$; they represent the incoherence of each target component with respect to other components as well as the noise. When the spatial separations between the individual target components are large enough, the following orthogonality condition prevails [similar to the condition in Eq. (23)]:

$$\sum_{m=-\infty}^{\infty} \int_{-\infty}^{\infty} d\tau s_i^\dagger(m - m_i, \tau - \tau_i) \cdot s_j(m - m_j, \tau - \tau_j) \approx 0 \quad (29)$$

for any two components located at different positions. Furthermore, the radar return from a specular or trihedral reflector is approximately orthogonal to that from a dihedral or tophat reflector due to the fact that the radar return wave from a specular or trihedral reflector is odd bounced, while the radar return wave from a dihedral or tophat reflector is even bounced. Table 2 enlists the correlation of the complex radar-return waveforms corresponding to a specular, dihedral (with 0, 45, or 90-deg orientation angle), tophat, and trihedral reflector, all with the edge length of one meter. The numerical values in Table 2 confirm that the specular and trihedral returns are approximately orthogonal to the dihedral and tophat returns.

We can develop a target classifier for a repertoire of multicomponent targets based on the single-target detectors. Based on a MAP rule, a single-target detector can be constructed by passing the radar-return signal through a bank of matched filters (matched to all target reflectors) and then combining the outputs from the matched filters. Specifically, the likelihood ratio for MAP target detection is

$$l_1(\mathbf{s}) = \frac{P_{\mathbf{r}|H_1}(r_1, r_2, \dots, r_M|H_1)}{P_{\mathbf{r}|H_0}(r_1, r_2, \dots, r_M|H_0)} = \prod_{m=1}^M \exp[-E_m] I_0(2|r_m|), \quad (30)$$

where hypothesis H_0 means the target is absent, H_1 means the target is present, E_m is the energy of the m 'th component return, and I_0 is the zero-order modified Bessel function. Here, \mathbf{r} is the vector of the matched filter outputs sampled at the proper times; it has complete information about the whole radar-return signal needed for the classification operation. At the target detector's output stage, a value equal or proportional to the likelihood ratio is compared with a threshold level to decide on the absence or presence of that target. When there is more than one possible target type, we can pass the radar return through a bank of target detectors, one for each target type. The resulting real-valued output levels l_1, \dots, l_N are the likelihood ratios of conditions H_1, \dots, H_N with respect to condition H_0

Table 2 Correlation coefficients of various target waveforms. The correlation coefficient of two complex waveforms is defined to be the magnitude of the inner product (the integral over the product of the first waveform times the complex conjugate of the second waveform) divided by the square root of the product of the first waveform's energy times the second waveform's energy. The upper panel corresponds to the spotlight mode, and the lower panel corresponds to the stripmap mode. All reflectors have the dimension of 1 m.

	Specular	Dihedral 0 deg	Dihedral 45 deg	Dihedral 90 deg	Trihedral 0 deg	Tophat
Specular	1.0	0.0021	0.0017	2.924×10^{-4}	0.1205	1.3271×10^{-4}
Dihedral 0 deg	0.0021	1.0	0.6499×10^{-6}	0.1583	5.0318×10^{-4}	0.1327
Dihedral 45 deg	0.0017	6.6499×10^{-6}	1.0	6.2463×10^{-5}	6.3453×10^{-4}	3.1767×10^{-4}
Dihedral 90 deg	2.9242×10^{-4}	0.1583	6.2463×10^{-5}	1.0	0.0012	0.2468
Trihedral 0 deg	0.1205	5.0318×10^{-4}	6.3453×10^{-4}	0.0012	1.0	8.9602×10^{-4}
Tophat	1.3271×10^{-4}	0.1327	3.1767×10^{-4}	0.2468	8.9602×10^{-4}	1.0
	Specular	Dihedral 0 deg	Dihedral 45 deg	Dihedral 90 deg	Trihedral 0 deg	Tophat
Specular	1.0	0.0021	0.0018	7.5001×10^{-4}	0.2577	3.6844×10^{-4}
Dihedral 0 deg	0.0021	1.0	8.0428×10^{-6}	0.3711	0.0011	0.3668
Dihedral 45 deg	0.0018	8.0428×10^{-6}	1.0	7.7375×10^{-6}	0.0015	2.6140×10^{-4}
Dihedral 90 deg	7.5001×10^{-4}	0.3711	7.7375×10^{-6}	1.0	0.0034	0.9572
Trihedral 0 deg	0.2577	0.0011	0.0015	0.0034	1.0	0.0013
Tophat	3.6844×10^{-4}	0.3668	2.6140×10^{-4}	0.9572	0.0013	1.0

(clutter and noise only). To carry out classification, we select their maximum value: if l_p is maximum among l_1, \dots, l_N , then the classifier decides the target to be type p .

Evaluation of the performance of multicomponent target classification is computationally intensive, because the likelihood values of different multicomponent targets are densely correlated in general. Within the scope of this work, we assume that each target component can be located anywhere, provided the orthogonality condition in Eq. (29) holds. For the upper bound and the lower bound on the probability of correct classification (PCC) developed in this section, the target components are assumed to be fixed at known positions, and the phase of the target signal from each component is randomly distributed in a uniform fashion, which represents the unavailability of accurate relative phase information between the various components of a multireflector target. The radar-return model under this target condition is specified by Eq. (28), and the time delays corresponding to the target component locations (m_{p^k}, τ_{p^k}) are presumed known.

4.2 Lower Bound on the Probability of Correct Classification

A lower bound on the PCC can be calculated by finding the PCC for any suboptimal classifier. For a suboptimal classifier, we use a component-wise detection rule. Suppose that the components are mutually orthogonal and that four reflector types (specular, dihedral, trihedral, and tophat) are considered. Then, we can carry out a binary detection (a reflector of any type versus a null) for each reflector component, and use these component decisions as inputs to a (suboptimum) MAP N -ary decision rule. We can regard the decision for each target component as establishing a binary

discrete memoryless channel (DMC), with transition probabilities calculated from the model in Fig. 9.

Combining the transition probabilities of the DMC with an N -ary decision rule based on the DMC then yields an easily calculated error probability from which a PCC lower bound immediately follows. This method of obtaining a lower bound on the PCC can also be applied to the conventional full-resolution imager.

4.3 Upper Bound on the Probability of Correct Classification

Obtaining an upper bound on the PCC is equivalent to finding a lower bound on the error probability. If the reflector phases were exactly known and optimally employed, then the error probability would not be higher than the case in which the phases of all components are random. Given exact phases, the classification problem simply becomes an N -ary detection of the signals in an additive white Gaussian noise channel. In general, the error probability of detection of N signals over the additive white Gaussian noise channel is not available in a closed form. Thus, we again use a lower bound on this error probability.

$$\begin{aligned}
 \text{PCC} &= \sum_{i=1}^N \Pr(\text{say } H_i | H_i \text{ true}) \Pr(H_i) \\
 &= \sum_{i=1}^N \{1 - \Pr(\text{error} | H_i \text{ true})\} \Pr(H_i).
 \end{aligned} \tag{31}$$

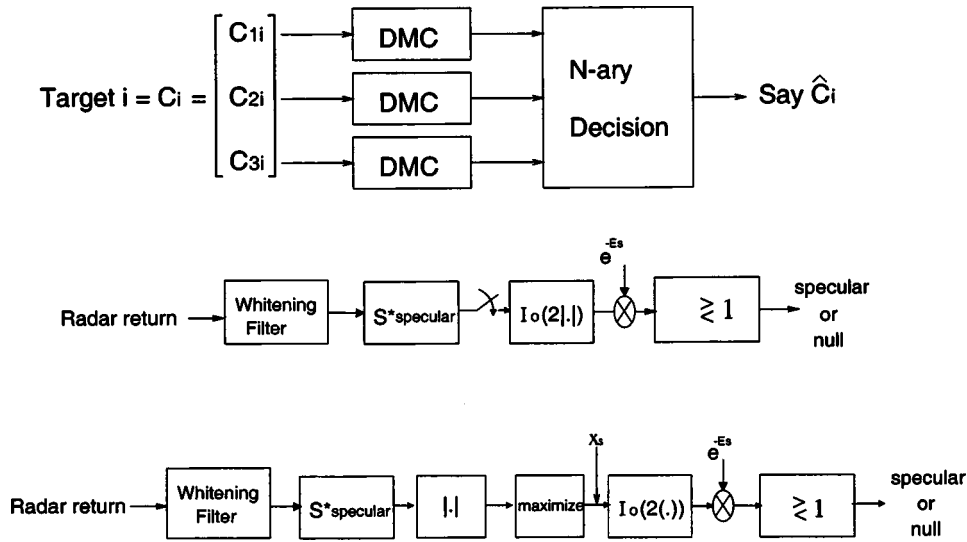


Fig. 9 The component-wise classifier for the multicomponent targets with 1. unknown phases and 2. unknown phases and positions. The upper panel is the overall architecture; the middle panel is the DMC for targets with unknown phases; and the lower panel is the DMC for the targets with unknown phases and positions.

$$\begin{aligned} & \Pr(\text{error} | H_i \text{ true}) \\ & \geq \Pr(\text{error} | H_i \text{ true, phase information given}) \\ & = \Pr\left(\bigcup_{j \neq i} \mathcal{E}_{ij} | H_i \text{ true, phase information given}\right). \end{aligned} \quad (32)$$

Here \mathcal{E}_{ij} denotes the case $\{\|s' - s_j\| \leq \|s' - s_i\|\}$, where s' is a matched-filter-output vector, matched to all distinct target components, and properly normalized to make the noise part circulo-complex Gaussian with unit variance. s_i is the mean of s' when the target i is present. The prior probability of target i , $\Pr(H_i)$, is assumed to be $1/N$, i.e., all targets will be assumed equiprobable.

De Caen's inequality³² can be used to get a lower bound on the probability of a union:

$$\Pr\left(\bigcup_{j=1}^N A_j\right) \geq \sum_j \frac{\Pr(A_j)^2}{\sum_k \Pr(A_j \cap A_k)}. \quad (33)$$

For $j=1$ to N , A_j is a subset of the sample space. Applying this inequality to the probability of error, we obtain

$$\begin{aligned} & \Pr(\text{error} | H_i \text{ true, phase information given}) \\ & \geq \sum_{j \neq i} \frac{Q^2(d_{ij}/2)}{\sum_{k \neq i} \Psi(\rho_{jk}, d_{ij}/2, d_{ik}/2)}, \end{aligned} \quad (34)$$

where

$$d_{ij} = \|s_i - s_j\|, \quad \rho_{jk} = \frac{\langle s_i - s_j, s_i - s_k \rangle}{\|s_i - s_j\| \|s_i - s_k\|},$$

$$Q(x) = \frac{1}{\sqrt{2\pi}} \int_x^\infty \exp(-y^2/2) dy,$$

$$\begin{aligned} & \Psi(\rho_{jk}, d_{ij}/2, d_{ik}/2) \\ & = \frac{1}{2\pi(1-\rho_{jk}^2)^{1/2}} \\ & \quad \times \int_{d_{ij}/2}^\infty \int_{d_{ik}/2}^\infty \exp\left[-\frac{x^2 - 2\rho_{jk}xy + y^2}{2(1-\rho_{jk}^2)}\right] dx dy. \end{aligned}$$

This inequality deals with only two joint Gaussian random variables, and we have all the constants needed for its evaluation, namely the distances between all signal points. The error probability bound is thus easy to calculate. Like the lower bound on the PCC, this upper bound can be applied to all processor models and both SAR operation modes.

4.4 Numerical Results

Consider the target recognition problem for four targets, each consisting of 9 or 10 reflectors with different locations, orientations, sizes, and types, as specified in Table 3. We apply the upper and lower bounds on PCC that we derived in the previous sections to this target constellation, using the system parameters given in Table 1. Figure 10 plots the PCC bounds versus the inverse of the CNR for both the conventional classifier and the optimal whitening-filter processor when both have a perfect knowledge of target location. Also included in this figure are PCC results obtained from Monte Carlo simulations of these two processors. Figure 10 shows that the PCC lower bound for the whitening-filter processor is close to its simulation result. For the conventional processor, the simulation shows that the PCC approaches a subunity, clutter-limited value in the limit of zero noise, i.e., when $1/\text{CNR} \rightarrow 0$. It also shows that the whitening-filter classifier has about 5-dB gain in terms of the SNCR as compared with the conventional processor. This advantage is due to the combined benefits accruing

Table 3 Specification of target constellation. Note that (x, y) is the center location (in meters), θ, ϕ are polar and azimuthal angles (deg), and ρ is half the side length of a reflector (in centimeters). S, D, Tr, and To in columns denoted by t stand for specular, dihedral, trihedral, and tophat reflector, respectively. The different sets of trihedral orientation angles denoted by $a, b, c, d, e,$ and f mean: $a: \theta=$ a rotation around the $(\hat{x}_b + \hat{y}_b)/\sqrt{2}$ axis=1 deg, $\psi=$ a rotation around the $(-\hat{x}_b + \hat{y}_b)/\sqrt{2}$ axis=0.5 deg; $b: \theta=-0.5$ deg, $\psi=1.5$ deg; $c: \theta=-1.5$ deg, $\psi=0$ deg; $d: \theta=1$ deg, $\psi=-1$ deg; $e: \theta=1.3$ deg, $\psi=-2.1$ deg; and $f: \theta=-0.3$ deg, $\psi=1.9$ deg.

Target 1				Target 2				Target 3				Target 4			
x, y	θ, ϕ	ρ	t	x, y	θ, ϕ	ρ	t	x, y	θ, ϕ	ρ	t	x, y	θ, ϕ	ρ	t
2.5 -0.2	a	5	Tr	-2.7 -0.7	-88 46	4	S	2.5 -0.2	a	5	Tr	-2.7 -0.7	-88 46	4	S
0.6 -0.5	b	4	Tr	0.6 -0.5	b	4	Tr	0.3 1.4	-90 43	10	D	0.6 -0.5	b	4	Tr
-2.0 -1.5	-90 45	9	S	-0.2 -0.5	...	16	To	-0.2 -0.5	...	16	To	-0.2 -0.5	...	16	To
-1.0 0.6	c	15	Tr	-0.6 -1.0	-93 43	6	D	2.0 1.0	-90 45	16	S	2.0 1.0	-90 45	16	S
-2.5 -0.8	...	5	To	-2.5 -0.8	...	5	To	-1.2 1.3	-88 44	10	S	-2.5 -0.8	...	5	To
1.2 -1.6	d	8	Tr	1.2 -1.6	d	8	Tr	-1.5 1.0	-90 45	13	D	1.2 -1.6	c	8	Tr
3.0 -1.5	-90 45	16	S	-0.7 -0.1	-85 43	19	D	-0.7 -0.1	-85 43	19	D	3.0 -1.5	-90 45	16	S
0.6 -0.7	...	6	To	2.7 -1.0	e	13	Tr	2.7 -1.0	e	13	Tr	0.6 -0.7	...	6	To
1.5 -1.0	f	8	Tr	0.2 -1.5	-90 49	9	D	1.5 -1.0	f	8	Tr	0.2 -1.5	-90 49	9	D
-0.6 1.4	-90 44	15	S												

from whitening-filter processing (which optimally suppresses clutter), full polarimetric processing (which only the optimal processor was presumed to have), and adaptive-resolution processing (which the optimal system uses to exploit physics-based signatures of the various reflector

components). In the noise-dominant condition under which the clutter plus noise is close to white, the whitening filter has little effect. The maximum polarimetric gain for a single reflector is up to 3 dB (usually identical HH and VV terms exist for single-bounced returns, while only the HV

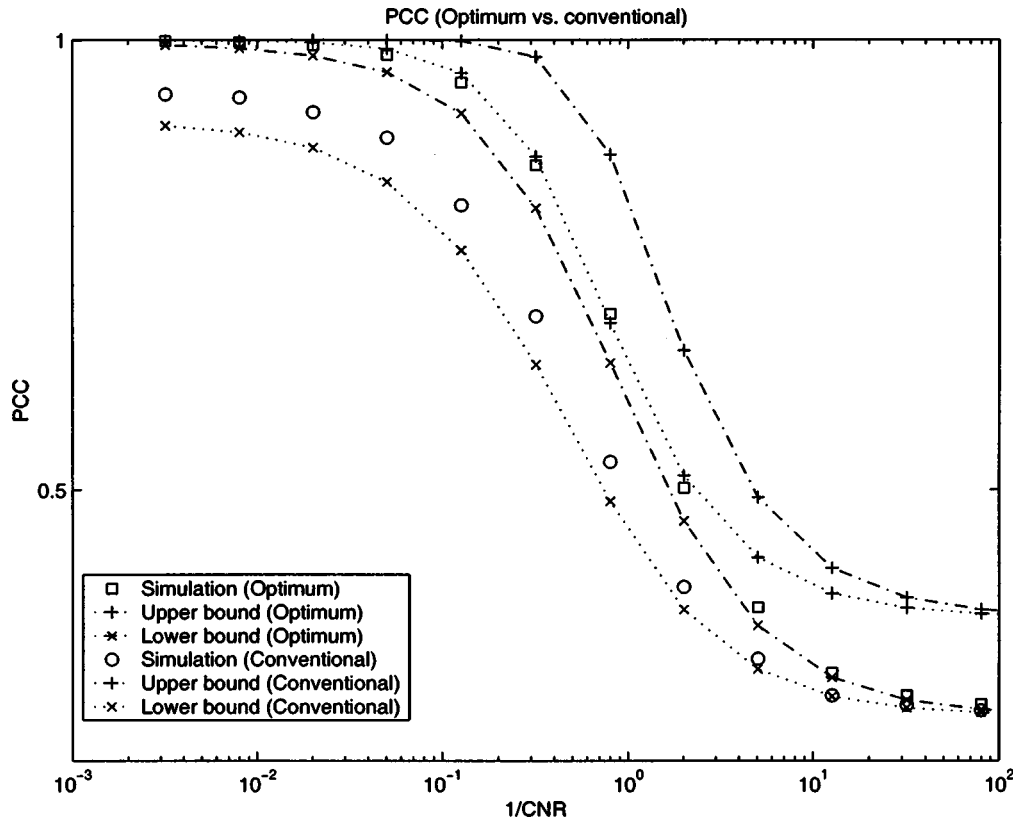


Fig. 10 Optimal processor and conventional processor PCC upper and lower bounds for the target constellation specified in Table 3 when target locations are known. Also included are the results of 50000-trial computer simulations of these two processors.

term exists for double-bounced returns). So the adaptive-resolution contribution is greater than 2 dB, comparable to the polarimetric contribution.

5 Multicomponent Target Classification with Uncertain Reflector Positions

In this section, we extend the target classification and PCC evaluation schemes developed in the previous section to multicomponent targets with uncertain positions.

5.1 Classification Scheme

First, we explore the classification of the targets with uncertain reflector positions. Incorporating the position uncertainty of the reflector components, the radar return for each hypothesis is modeled in the same form as that in Eq. (28), except the center locations (m_{p^k}, τ_{p^k}) of the target components are no longer fixed and known. The random variables m_{p^k}, τ_{p^k} are assumed to be mutually independent and each random variable is uniformly distributed within $[m_{p^k}^0 - M_{p^k}/2, m_{p^k}^0 + M_{p^k}/2]$ for m_{p^k} , and $[\tau_{p^k}^0 - T_{p^k}/2, \tau_{p^k}^0 + T_{p^k}/2]$ for τ_{p^k} . The position randomness models the variability or unavailability of the exact knowledge about some aspects of a target reflector constellation in the real world.

Because the delay times are uniform random variables, it is difficult to write down the likelihood ratio of two different hypotheses. We can, however, formulate the GLR and develop a target classifier on that basis. For a specific realization of the delay times, the likelihood ratio of hypotheses H_k (target k) with respect to the null hypotheses H_0 (clutter plus noise only) is:

$$l_k(\mathbf{s}; m_1, \dots, m_{M_k}, \tau_1, \dots, \tau_{M_k}) = \frac{p_{\mathbf{r}|H_k}(r_1, r_2, \dots, r_{M_k} | H_k; m_1, \dots, m_{M_k}, \tau_1, \dots, \tau_{M_k})}{p_{\mathbf{r}|H_0}(r_1, r_2, \dots, r_{M_k} | H_0; m_1, \dots, m_{M_k}, \tau_1, \dots, \tau_{M_k})} = \prod_{p=1}^{M_k} \exp(-E_{p^k}) I_0 \left[2 \left| \sum_m \int_{-\infty}^{\infty} d\tau \times \mathbf{s}_{p^k}^\dagger(m - m_{p^k}, \tau - \tau_{p^k}) \cdot \mathbf{r}(m, \tau) \right| \right], \quad (35)$$

where E_{p^k} is the energy of the p 'th component of the k 'th target. For a given radar return $\mathbf{r}(m, \tau)$, the likelihood ratio is a function of $m_1, \dots, m_{M_k}, \tau_1, \dots, \tau_{M_k}$. The maximum likelihood estimate of these parameters from the radar return is:

$$[\hat{m}_1 \dots \hat{m}_{M_k} \hat{\tau}_1 \dots \hat{\tau}_{M_k}] = \arg \max \prod_{p=1}^{M_k} \exp(-E_{p^k}) I_0 \left[2 \left| \sum_m \int_{-\infty}^{\infty} d\tau \times \mathbf{s}_{p^k}^\dagger(m - m_{p^k}, \tau - \tau_{p^k}) \cdot \mathbf{r}(m, \tau) \right| \right], \quad (36)$$

where $\hat{m}_1, \dots, \hat{m}_{M_k}, \hat{\tau}_1, \dots, \hat{\tau}_{M_k}$ are the maximum likelihood estimates over $m_1 \in [m_1^0 - M_1/2, m_1^0 + M_1/2], \dots, m_{M_k}$

$\in [m_{M_k}^0 - M_{M_k}/2, m_{M_k}^0 + M_{M_k}/2]$ and $\tau_1 \in [\tau_1^0 - T_1/2, \tau_1^0 + T_1/2], \dots, \tau_{M_k} \in [\tau_{M_k}^0 - T_{M_k}/2, \tau_{M_k}^0 + T_{M_k}/2]$. The GLR is defined as the likelihood ratio when the unknown parameters are replaced by their maximum likelihood estimates. Plugging Eq. (36) into Eq. (35), we have that:

$$\text{GLR} = l_k(\mathbf{r}; \hat{m}_1, \dots, \hat{m}_{M_k}, \hat{\tau}_1, \dots, \hat{\tau}_{M_k}) = \max \prod_{p=1}^{M_k} \exp(-E_{p^k}) I_0 \left[2 \left| \sum_m \int_{-\infty}^{\infty} d\tau \times \mathbf{s}_{p^k}^\dagger(m - m_{p^k}, \tau - \tau_{p^k}) \cdot \mathbf{r}(m, \tau) \right| \right]. \quad (37)$$

The GLR detector based on Eq. (37) can be written in the following form:

$$\max \prod_{p=1}^{M_k} \left\{ I_0 \left[2 \left| \sum_m \int_{-\infty}^{\infty} d\tau \times \mathbf{s}_{p^k}^\dagger(m - m_{p^k}, \tau - \tau_{p^k}) \cdot \mathbf{r}(m, \tau) \right| \right] \right\} \begin{array}{l} \text{say } H_k \\ > \\ < \\ \text{say } H_0 \end{array} \beta, \quad (38)$$

where β is the threshold and the maximum is over the same domain as that in Eq. (37). Furthermore, because the zero-order modified Bessel function is monotonically increasing and $m_1, \dots, m_{M_k}, \tau_1, \dots, \tau_{M_k}$ are mutually independent variables, maximizing the overall product of I_0 in Eq. (38) is equivalent to maximizing each I_0 in the product. Hence the GLR detector becomes

$$\prod_{p=1}^{M_k} \max \left\{ I_0 \left[2 \left| \sum_m \int_{-\infty}^{\infty} d\tau \times \mathbf{s}_{p^k}^\dagger(m - m_{p^k}, \tau - \tau_{p^k}) \cdot \mathbf{r}(m, \tau) \right| \right] \right\} \begin{array}{l} \text{say } H_k \\ > \\ < \\ \text{say } H_0 \end{array} \beta. \quad (39)$$

The form of the GLR detector is similar to the LR detector discussed in the previous section, except that in the GLR detector the value used to compare with the threshold is maximized over the region of the delay time uncertainty. This operation can be achieved by inserting a duration-limited peak detector after the video detection of the output from each individual matched filter. A target classifier can be built, as discussed in the previous section, by employing a bank of target detectors, incorporating energy corrections, and choosing the largest output level.

To calculate the PCC for the N -ary target recognition problem, we need to obtain the statistical structure of the GLR. As implied by Eq. (39), to obtain the statistics of the GLR we must solve the following general level-crossing problem: for a complex 2-D random process with a given covariance function and a fixed real-valued threshold level, what is the probability that the magnitude of this random process is smaller than the threshold level within a given area? When the target is absent or all the components are mismatched to the detector's filters, then this random pro-

cess is approximately stationary. When at least one of the target components is matched to the detector's filters, this process is nonstationary. As a result it is best to consider the level-crossing problems for H_0 and H_k ($k \neq 0$) separately.

5.2 Lower Bound on the PCC

Paralleling the work in the last section, a component-wise detector can be exploited to obtain a lower bound on the PCC for the random-position case. Any suboptimal classifier will be inferior in its classification performance to the optimum one. Thus, the PCC for a suboptimal target recognizer is a valid PCC lower bound for an optimum classifier.

A component-wise detector can be used in the optimum target detector for a single-reflector target. We discriminate the reflector type for each component separately, and then collect the results from each component-wise detector to make a MAP N -ary decision. This is a valid classification scheme, but not necessarily the optimum one. To obtain the PCC for this suboptimal classifier, we only need to know the transition probabilities for the component-wise detector. Assume the true target component is specular. We have that the transition probability, $Q_1 \equiv \Pr(\text{say specular} | \text{specular is true})$, satisfies

$$\begin{aligned} Q_1 &= \Pr(l_s > l_0 = 1 | \text{specular is true}) \\ &= \Pr[I_0(2x_s)\exp(-E_s) > 1 | \text{specular is true}] \\ &= \Pr\{x_s > \frac{1}{2}I_0^{-1}[\exp(E_s)] | \text{specular is true}\} \\ &= 1 - \Pr(x_s < \gamma | \text{specular is true}), \end{aligned} \tag{40}$$

where $\gamma = I_0^{-1}[\exp(E_s)]/2$, and x_s is the output from the maximum finder of the detector for the target with an unknown location (see Fig. 9).

To evaluate the last term, we need to know the probability structure of x_s . The radar return is passed through a filter that is matched to that of the specular return signal. The maximization process will pick up the peak value of the magnitude of the postmatched-filter signal within the uncertainty region. If we partition the uncertainty region into resolution bins and assume that each bin is statistically independent of the others, we can formulate the cumulative distribution function (CDF) of x_s as follows:

$$\Pr(x_s < \gamma | \text{specular is true}) = P_1^{N_b-1}(\gamma)P_2(\gamma), \tag{41}$$

where N_b is the number of bins, $P_1(\gamma)$ is the probability that the magnitude of the stationary whitened clutter-plus-noise is always less than γ for a given bin area, and $P_2(\gamma)$ is the CDF of the output value from a perfectly matched signal sampled at the correct position. $P_1(\gamma)$ can be calculated by applying 2-D level-crossing theory, and $P_2(\gamma)$ can be obtained analytically. Since we know the statistics of x_s , we can now evaluate the transition probability Q_1 .

To calculate a transition probability, $Q_2 \equiv \Pr(\text{say specular} | \text{no reflector is present})$, we need to know the statistics of x_s that is the radar return from clutter only, matched to the specular signal. Thus, x_s will be stationary

over the whole uncertainty region. We can, again, apply the 2-D level-crossing theory to obtain the CDF of x_s .

$$\begin{aligned} Q_2 &= \Pr(x_s > \frac{1}{2}I_0^{-1}[\exp(E_s)] | \text{no reflector is present}) \\ &= 1 - P_1^{N_b}(\gamma), \end{aligned} \tag{42}$$

where $\gamma = I_0^{-1}[\exp(E_s)]/2$. We can find all other transition probabilities in a similar way. Having all the transition probabilities, we can make an N -ary decision based on the MAP rule and obtain our component-wise lower bound on the PCC for the case of position uncertainty.

5.3 Upper Bound on the PCC

To get an upper bound on the PCC, we assume that we have exact phase information for each reflector. Because this means we have more information for the classification task, the PCC for the optimum receiver in this case will be a valid upper bound on the PCC in the case of target with random phases, which we are interested in. If we assume all target components are orthogonal, we can set the phases to be zero for all target component signals without loss of generality. Thus the formula for the radar return signal is similar to Eq. (28), except that all $\exp(i\phi_p)$ terms are left out. Using this return signal model, the likelihood ratio for the target k with respect to target 0 (the null hypothesis) is:

$$\begin{aligned} l_k(\mathbf{r}; m_1, \dots, m_{M_k}, \tau_1, \dots, \tau_{M_k}) \\ &= \prod_{p=1}^{M_k} \exp\left(-E_{p^k} + 2\Re\left\{\sum_m \int_{-\infty}^{\infty} d\tau \right. \right. \\ &\quad \left. \left. \times \mathbf{s}_{p^k}^\dagger(m - m_{p^k}, \tau - \tau_{p^k}) \cdot \mathbf{r}(m, \tau)\right\}\right), \end{aligned} \tag{43}$$

where E_{p^k} is the energy of the p 'th component of the k 'th target, and \Re denotes the real part. The appearance of the $\Re(g)$ (g denotes the argument of the \Re operator) is due to the fact that the probability density function $p(\mathbf{r} | \mathbf{H}_k)$ has the exponent $E_{p^k}g + (E_{p^k}g)^*$ and E_{p^k} is real. The equation is similar to Eq. (35) but does not involve a Bessel function. The generalized log likelihood ratio (GLLR) for the target k is thus:

$$\begin{aligned} \text{GLLR}_k &= \sum_{p=1}^{M_k} \left(-E_{p^k} + 2 \max \Re\left\{\sum_m \int_{-\infty}^{\infty} d\tau \right. \right. \\ &\quad \left. \left. \times \mathbf{s}_{p^k}^\dagger(m - m_{p^k}, \tau - \tau_{p^k}) \cdot \mathbf{r}(m, \tau)\right\}\right) \\ &= \sum_{p=1}^{M_k} (-E_{p^k} + 2y_{p^k}). \end{aligned} \tag{44}$$

Here, the statistics of y_{p^k} can be calculated via level-crossing theory. The probability of correct classification can then be evaluated via

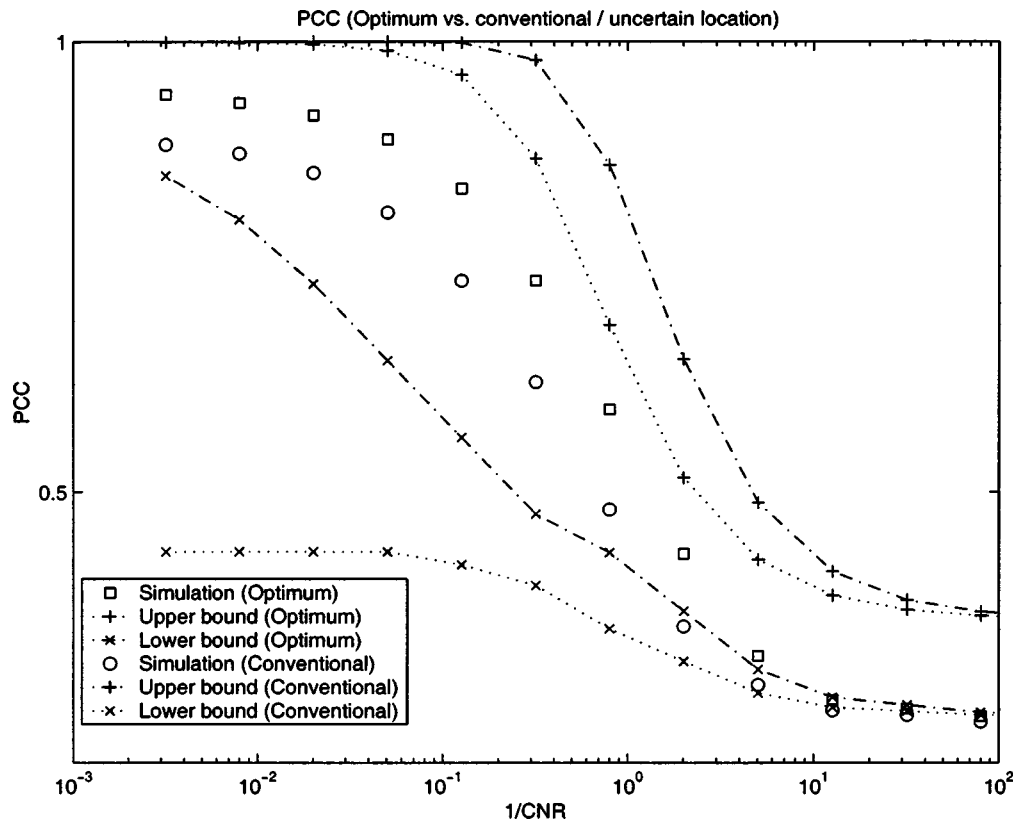


Fig. 11 Optimal processor and conventional processor PCC upper and lower bounds for the target constellation specified in Table 3 when the target reflector locations are not known. Also included are the results of 50000-trial computer simulations of these two processors.

$$\begin{aligned}
 &PCC|H_i = 1 - \Pr(\text{error}|H_i \text{ is true}) \\
 &\leq 1 - \Pr(\text{error}|H_i \text{ is true, phase information given}) \\
 &= 1 - \Pr\left(\bigcup_{j \neq i} \{GLLR_i < GLLR_j\} \mid H_i \text{ is true, phase info given}\right) \\
 &\leq 1 - \max_{j \neq i} \Pr(GLLR_i < GLLR_j | H_i \text{ is true, phase info given}). \quad (45)
 \end{aligned}$$

In the previous section we used de Caen’s inequality in Eq. (33) to obtain a tighter lower bound on the probability of a union, which involves the joint probability distribution of two Gaussian random variables. However, for this target setting, we cannot apply de Caen’s inequality, because the statistics of $GLLR_i$ are complicated. The formula in Eq. (45) can be calculated without difficulty, since we have the statistics for the GLLRs.

5.4 Numerical Results

We obtained the lower and upper bounds on the PCC for the target setting specified in Table 3. Uncertain areas for the target reflectors were all set to squares with side length of 10 cm. Figure 11 compares the lower and upper bounds on the PCC for the optimum whitening classifier with re-

spect to those for the conventional classifier. It presents similar features to those seen earlier for the known reflector position example. Thus, although the PCC lower bound for the whitening processor is somewhat looser when compared with the simulation result, the optimal classifier still has about 5-dB SNCR gain relative to the conventional classifier. Note that there is a considerable gap, for the conventional processor, between the PCC lower bound and the simulation result, and neither of these curves approaches unity as $1/CNR \rightarrow 0$, for the clutter appearing in the conventional processor is not as small as that in the optimum processor when the noise is diminishing. Figure 12 compares the whitening processor’s PCC simulations for the cases of known and unknown reflector locations. In this example, the uncertainty of reflector locations results in a 3- to 5-dB SNCR penalty.

6 Conclusion

We develop a physics-based target recognition theory for SAR images. The basic idea is to construct radar-return signatures from electromagnetic scattering theory, and to apply conventional SAR processors and likelihood-ratio optimum processors to perform detection or classification based on these radar signatures. The contribution of this study is not one of new efficient or powerful processing schemes for real radar data or complicated target signatures generated from CAD models. Instead, it theoretically quantifies the target-recognition performance improvement of

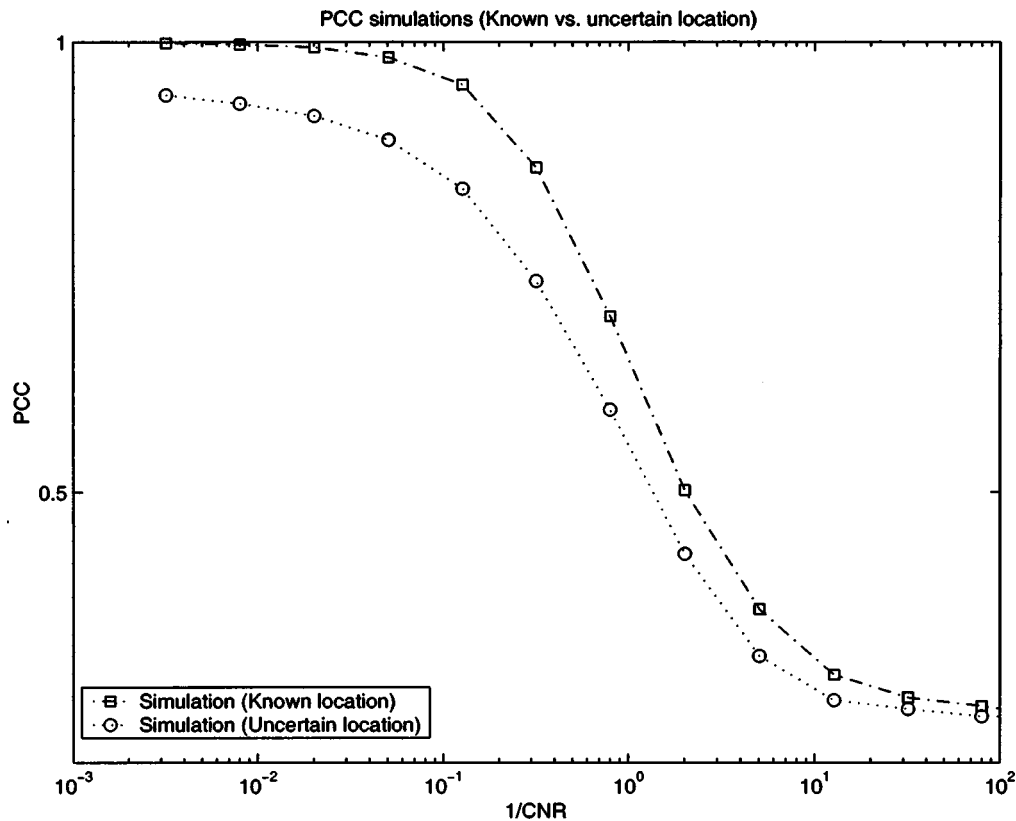


Fig. 12 Comparison of optimal processor PCC simulations for the cases of known and unknown reflector locations.

adaptive-resolution, polarimetric, or whitening-filter processing, and provides physical interpretations for such advantages.

The performance analysis for likelihood-based processors for multicomponent target detectors shows that the fully polarimetric Neyman-Pearson processor has better detection performance than the scalar Neyman-Pearson (adaptive-resolution) processor, which has performance superior to that of the conventional SAR processor. We discovered that the effect of adaptive resolution can be important when the reflector size is much larger (for both stripmap and spotlight mode) or smaller (for spotlight mode) than the diameter of antenna aperture. The performance analysis for multicomponent target classifiers also indicates that the Neyman-Pearson processor outperforms the conventional SAR processor for a richer reflector repertoire and a more complex target scenario: a significant SNCR gain of about 5 dB. According to our estimation, the optimum likelihood-ratio processor's adaptive-resolution and polarimetric effects are comparable when the whitening-filter effect is negligible. We also found that the binary discrete-memoryless-channel processor has quite close classification performances to those of the optimum processor, especially when the target locations are known.

Acknowledgments

This research was supported by U.S. Air Force Office of Scientific Research Grant F49620-96-1-0028.

References

1. L. M. Novak, S. D. Halversen, G. J. Owirka, and M. Hielt, "Effects of polarization and resolution on the performance of a SAR automatic target recognition system," *Lincoln Lab. J.* **8**(1), 49–68 (1995).
2. H. R. Park, J. Li, and H. Wang, "Polarization-space-time domain generalized likelihood ratio detection of radar targets," *Signal Process.* **41**, 153–164 (1995).
3. M. W. Tu, I. J. Gupta, and E. K. Walton, "Application of maximum likelihood estimation to radar imaging," *IEEE Trans. Antennas Propag.* **45**(1), 20–27 (1997).
4. T. Soni, J. R. Zeidler, and W. H. Ku, "Performance evaluation of 2-D adaptive prediction filters for detection of small objects in image data," *IEEE Trans. Image Process.* **2**(3), 327–340 (1993).
5. W. Irving, R. B. Washburn, and W. E. L. Grimson, "Bounding performance of peak-based target detectors," *Proc. SPIE* **3070**, 245–257 (1997).
6. J. S. Lee and K. Hoppel, "Principal components transformation of multifrequency polarimetric SAR imagery," *IEEE Trans. Geosci. Remote Sens.* **30**(4), 686–696 (1992).
7. L. M. Novak, M. C. Burt, R. D. Chaney, and G. J. Owirka, "Optimal processing of polarimetric synthetic-aperture radar imagery," *Lincoln Lab. J.* **3**(2), 273–290 (1990).
8. J. A. O'Sullivan and M. D. DeVore, "Performance-complexity tradeoffs for several approaches to ATR from SAR images," *Proc. SPIE* **4053**, 587–597 (2000).
9. J. A. O'Sullivan, M. D. DeVore, V. Kedia, and M. I. Miller, "SAR ATR performance using a conditionally Gaussian model," *IEEE Trans. Aerosp. Electron. Syst.* **37**(1), 91–106 (2001).
10. X. Yu, L. E. Hoff, I. S. Reed, A. M. Chen, and L. B. Stotts, "Automatic target detection and recognition in multiband imagery: a unified ML detection and estimation approach," *IEEE Trans. Image Process.* **6**(1), 143–156 (1997).
11. S. Krishnamachari and R. Chellapa, "Multiresolution Gauss-Markov random field models for texture segmentation," *IEEE Trans. Image Process.* **6**(2), 251–267 (1997).
12. A. H. S. Solberg, T. Taxt, and A. K. Jain, "A Markov random field model for classification of multisource satellite imagery," *IEEE Trans. Geosci. Remote Sens.* **34**(1), 100–113 (1996).
13. W. W. Irving, L. M. Novak, and A. S. Willsky, "A multiresolution

- approach to discriminating targets from clutter in SAR imagery," *Proc. SPIE* **2487**, 272–299 (1995).
14. R. D. Chaney, A. S. Willsky, and L. M. Novak, "Coherent aspect-dependent SAR image formation," *Proc. SPIE* **2230**, 256–274 (1994).
 15. N. S. Subotic, B. J. Thelen, J. D. Gorman, and M. F. Reiley, "Multi-resolution detection of current radar targets," *IEEE Trans. Image Process.* **16**(1), 21–35 (1997).
 16. D. C. Munson, J. D. O'Brien, and W. K. Jenkins, "A tomographic formulation of spotlight-mode synthetic aperture radar," *Proc. IEEE* **71**(8), 917–925 (1983).
 17. D. C. Munson and R. L. Visentin, "A signal-processing view of strip-mapping synthetic aperture radar," *IEEE Trans. Acoust., Speech, Signal Process.* **37**(12), 2131–2147 (1989).
 18. N. Nandhakumar and J. K. Aggarwal, "Physics-based integration of multiple sensing modalities for scene interpretation," *Proc. IEEE* **85**(1), 147–163 (1997).
 19. R. L. Moses, E. Erten, and L. C. Potter, "Performance analysis of anisotropic scattering center detection," *Proc. SPIE* **3070**, 235–244 (1997).
 20. L. C. Potter and R. L. Moses, "Attributed scattering centers for SAR ATR," *IEEE Trans. Image Process.* **6**(1), 79–91 (1997).
 21. D. Park, "High-resolution laser radar performance analysis," PhD Thesis, Department of Electrical Engineering and Computer Science, MIT (1988).
 22. D. Park and J. H. Shapiro, "Performance analysis of optical synthetic aperture radars," *Proc. SPIE* **999**, 100–116 (1988).
 23. G. Leung and J. H. Shapiro, "Toward a fundamental understanding of multiresolution SAR signatures," *Proc. SPIE* **3070**, 100–109 (1997).
 24. G. Leung, "Synthetic aperture radar discrimination of diffuse and specular target returns," MEng Thesis, Department of Electrical Engineering and Computer Science, MIT (1997).
 25. J. A. Kong, *Electromagnetic Wave Theory*, John Wiley and Sons, New York (1990).
 26. C.-P. Yeang, "Target identification theory for synthetic aperture radar images using physics-based signatures," ScD Thesis, Department of Electrical Engineering and Computer Science, MIT (1999).
 27. M. A. Richards and K. D. Trott, "A physical optics approximation to the range profile signature of a dihedral corner reflector," *IEEE Trans. Electromagn. Compat.* **37**(3), 478–481 (1995).
 28. L. Tsang, J. A. Kong, and R. T. Shih, *Theory of Microwave Remote Sensing*, John Wiley and Sons, New York (1985).
 29. W. G. Carrara, R. S. Goodman, and R. M. Majewski, *Spotlight Synthetic Aperture Radar: Signal Processing Algorithms*, Artech House, Boston (1995).
 30. C. W. Helstrom, *Statistical Theory of Signal Detection*, Pergamon Press, Elmsford, NY (1968).
 31. J. H. Shapiro, R. W. Reinhold, and D. Park, "Performance analyses for peak-detecting laser radars," *Proc. SPIE* **663**, 38–56 (1996).
 32. G. E. Séguin, "A lower bound on the error probability for signals in white Gaussian noise," *IEEE Trans. Inf. Theory* **44**(7), 3168–3175 (1998).



Chen-Pang Yeang received the BS degree in electrical engineering from the National Taiwan University in 1992, and the SM and ScD degrees in electrical engineering from the Massachusetts Institute of Technology in 1996 and 1999, respectively. As a graduate student, he was a research assistant at the MIT Research Laboratory of Electronics. His doctoral research was electromagnetics-based target recognition theory for synthetic aperture radar imagery.

Since 1999, he has been in the doctoral program of the History and

Social Studies of Science and Technology at MIT. His PhD dissertation topic is the history of radio science and engineering in the early twentieth century. He is currently a graduate fellow of the Dibner Institute for History of Science and Technology. In the summers of 2000 and 2001, he was a postdoctoral fellow at the MIT Laboratory of Information and Decision Systems. In 2002, he was a visiting scholar at the History Faculty of the California Institute of Technology. He is a member of IEEE and Sigma Xi.



Choongyeun Cho received the BS degree in electronics engineering in 1998 from Korea University, Seoul, and the SM degree in electrical engineering in 2001 from Massachusetts Institute of Technology (MIT), where he is currently pursuing the PhD degree in the Remote Sensing and Estimation Group.



Jeffrey Shapiro received the SB, SM, EE, and PhD degrees in electrical engineering from the Massachusetts Institute of Technology in 1967, 1968, 1969, and 1970, respectively. As a graduate student he was a National Science Foundation Fellow, a Teaching Assistant, and a Fannie and John Hertz Foundation Fellow. His doctoral research was a theoretical study of adaptive techniques for improved optical communication through atmospheric turbulence.

From 1970 to 1973, he was an assistant professor of electrical sciences and applied physics at Case Western Reserve University. From 1973 to 1985, he was an associate professor of electrical engineering at MIT, and in 1985, he was promoted to Professor of Electrical Engineering. From 1989 until 1999 he served as Associate Department Head. In 1999 he became the Julius A. Stratton Professor of Electrical Engineering. In 2001, he was appointed Director of MIT's Research Laboratory of Electronics. His research interests have centered on the application of communication theory to optical systems. He is best known for his work on the generation, detection, and application of squeezed-state light beams, but he has also published extensively in the areas of atmospheric optical communication and coherent laser radar. He is a fellow of IEEE, the Optical Society of America, and the Institute of Physics, and he is a member of the American Physical Society and SPIE. He has been an Associate Editor of the *IEEE Transactions on Information Theory* and the *Journal of the Optical Society of America*. He was the principal organizer of the Sixth International Conference on Quantum Communication, Measurement and Computing.